Chemical Science

ROYAL SOCIETY OF CHEMISTRY

EDGE ARTICLE

View Article Online
View Journal | View Issue



Cite this: *Chem. Sci.*, 2023, **14**, 6355

All publication charges for this article have been paid for by the Royal Society of Chemistry



# Air-stable four-coordinate cobalt(II) single-ion magnets: experimental and *ab initio* ligand field analyses of correlations between dihedral angles and magnetic anisotropy†

Sandeep K. Gupta, [a] Shashank V. Rao, [b] Serhiy Demeshko,[a] Sebastian Dechert, [a] Eckhard Bill,[c] Mihail Atanasov, *[bd] Frank Neese *[b] and Franc Meyer *[a]

For single-ion magnets (SIMs), understanding the effects of the local coordination environment and ligand field on magnetic anisotropy is key to controlling their magnetic properties. Here we present a series of tetracoordinate cobalt(II) complexes of the general formula $[^{F}L_2Co]X_2$ (where $^{F}L$ is a bidentate diamido ligand) whose electron-withdrawing $-C_6F_5$ substituents confer stability under ambient conditions. Depending on the cations X, these complexes adopt structures with greatly varying dihedral twist angle $\delta$ between the N–Co–N′ chelate planes in the solid state (48.0 to 89.2°). AC and DC field magnetic susceptibility measurements show this to translate into very different magnetic properties, the axial zero-field splitting (ZFS) parameter $D$ ranging from $-69$ cm$^{-1}$ to $-143$ cm$^{-1}$ with substantial or negligible rhombic component $E$, respectively. A close to orthogonal arrangement of the two *N*,*N*′-chelating σ- and π-donor ligands at the Co(II) ion is found to raise the energy barrier for magnetic relaxation to above 400 K. Multireference *ab initio* methods were employed to describe the complexes' electronic structures, and the results were analyzed within the framework of *ab initio* ligand field theory to probe the nature of the metal–ligand bonding and spin–orbit coupling. A relationship between the energy gaps of the first few electronic transitions and the ZFS was established, and the ZFS was correlated with the dihedral angle $\delta$ as well as with the metal–ligand bonding variations, *viz.* the two angular overlap parameters $e_\sigma$ and $e_{\pi s}$. These findings not only give rise to a Co(II) SIM showing open hysteresis up to 3.5 K at a sweep rate of 30 Oe s$^{-1}$, but they also provide design guidelines for Co(II) complexes with favorable SIM signatures or even switchable magnetic relaxation properties.

Received 13th February 2023
Accepted 12th May 2023

DOI: 10.1039/d3sc00813d

rsc.li/chemical-science

## Introduction

The observation of slow relaxation of the magnetization in a molecular complex, first discovered for the "$Mn_{12}$ acetate" cluster,[1] was an impactful landmark for interdisciplinary research in chemistry, physics, and materials science.[1,2] Such single-molecule magnets (SMMs) promised great potential for applications in the fields of high-density data storage, quantum computing, and spintronics.[2a,3] Furthermore, it was the first time quantum tunneling of the magnetization (QTM) was observed experimentally as steps in the magnetic hysteresis.[4] This, in addition to fundamental interest, spurred the development of multinuclear exchange-coupled paramagnetic complexes with a very high ground spin-state ($S$), since the energy barrier for spin reversal ($U_{eff}$) is given by $U_{eff} = |D|S^2$ (for integer spins) or $U_{eff} = |D|(S^2 - 1/4)$ (for half-integer spins).[5] Here $D$ is the axial zero-field splitting (ZFS) parameter, a measure of the magnetic anisotropy of the system. However, it was soon pointed out that maximization of $S$ does not always lead to a higher energy barrier because $D$ is inversely correlated with $S$.[6] This directed the research efforts towards maximizing $D$ in molecular complexes featuring large anisotropy, and ultimately towards single-ion magnets (SIMs).

For SIMs based on transition metal ions, Co(II) complexes are particularly prominent, but relatively few of them exhibit slow

[a]*Institut für Anorganische Chemie, Universität Göttingen, Tammannstrasse 4, 37077 Göttingen, Germany. E-mail: franc.meyer@chemie.uni-goettingen.de*

[b]*Max Planck Institut für Kohlenforschung, Kaiser-Wilhelm-Platz 1, 45470 Mülheim an der Ruhr, Germany. E-mail: mihail.atanasov@kofo.mpg.de; neese@kofo.mpg.de*

[c]*Max Planck Institute for Chemical Energy Conversion, Stiftstrasse 34-36, 45470 Mülheim an der Ruhr, Germany*

[d]*Institute of General and Inorganic Chemistry, Bulgarian Academy of Sciences, Akad. Georgi Bontchev Street 11, 1113 Sofia, Bulgaria*

† Electronic supplementary information (ESI) available: NMR, IR, UV-Vis and ESI mass spectra, cyclic voltammograms, crystallographic information, magnetic characterization, and details of the theoretical calculations. CCDC 2240414 (**1**), 2240415 (**2**), 2240416 (**3**), 2240417 (**5**) and 2240418 (**6**). For ESI and crystallographic data in CIF or other electronic format see DOI: https://doi.org/10.1039/d3sc00813d

relaxation dynamics in the absence of an applied magnetic field.[7] The extremely air-sensitive mononuclear Co(II) complex $[Co(SPh)_4][PPh_4]_2$ was the first reported zero-field 3d-SIM.[8] Since then several Co(II) SIMs with a coordination number ranging from two to six have been discovered.[8–14] However, some complexes with two,[9] three,[10a] four[8,11a–o] and six[13a–d] coordinate metal ions feature the most favorable properties, and the largest energy barriers for any 3d SIMs have been observed for linear two-coordinate complexes where the ligand field is weak, thus maximizing the orbital contribution to the magnetic moment.[9] Among the prominent examples of this family is the recently reported linear two-coordinate dialkyl Co(II) complex $Co(C(SiMe_2ONaph)_3)_2$ that exhibits a non-Aufbau ground state $L = 3$ with a limiting magnetic anisotropy for a Co(II) ion.[9b] This is comparable with magnetic anisotropy exhibited by mono-coordinate Co atoms deposited on a MgO surface.[15] However, these low coordinate complexes are extremely air and moisture sensitive.

Four-coordinate Co(II) complexes are usually more rugged than the low-coordinate complexes. In order to maximize the orbital contribution through second order spin–orbit coupling in distorted tetrahedral Co(II) complexes and increase the ZFS, which ultimately determines the magnetic anisotropy, great efforts are being made to understand the underlying factors that govern the magnitude of the ZFS and relaxation processes.[11a,b,q,16] In this context, magneto-structural correlations have been developed for four-coordinate Co(II) SIMs, allowing to rationalize the effects of the structural distortion around the central paramagnetic ion on the sign and magnitude of the ZFS (Chart 1).[11a–e,g,i,r,v,17] Most studied are four-coordinate $[Co^{II}X_4]^{2-}$ complexes where X is an O-, S-, Se-, or Te-donor based monodentate anionic ligand **A** in Chart 1.[11a–e] It has been shown that the magnitude and sign of $D$ are highly dependent on the nature of the donor atoms of the coordinating ligand X (*viz.*, O, S, Se or Te). π-Anisotropic ligand systems with decreasing ligand field strength, *i.e.*, with softer donor atoms, in tetragonally elongated $D_{2d}$ geometries lead to significantly enhanced negative $D$.[8,11a] Magneto-structural correlations for these $[Co^{II}X_4]^{2-}$ systems have been established mainly for two types of structural distortions. The first one relates to the distortion $2\gamma$ of the first coordination sphere (where $\gamma$ is the angle between the $S_4$-rotation axis and the Co–X bond) and the second one ($\omega$) describes torsion angles involving the second coordination sphere (R–S–Co–$S_4$ axis; **A** in Chart 1).[11a–e] Their analysis has revealed that a large negative $D$ value is associated with smaller $2\gamma$ values (tetragonal elongation) and the maximum negative $D$ is achieved for $\omega = 0°$. Similar magneto-structural correlations have been reported for $CoL_2X_2$ systems (**B** in Chart 1, L = neutral donor ligands and X = anions).[18] Variations of the donor atom/coordinating anions in $CoL_2X_2$ systems have provided additional insights, indicating that the heavier and softer donor atoms significantly enhance the ZFS in Co(II) SIMs.[11k,17e,19] Lately, there has been interest in understanding the effect of molecular vibrations concerning the relaxation mechanism operating in SIMs as well.[16c,d]

In addition to $[CoX_4]^{2-}$ or $CoL_2X_2$ systems with monodentate ligands, enhanced magnetic bistability has recently been reported for four-coordinate Co(II) complexes derived from bidentate chelate ligands (**C** and **D** in Chart 1, and **E** and **F** in Chart 2).[11f–j,11p,q] In 2015, some of us found appreciable single-ion anisotropy ($D = -58$ cm$^{-1}$) and slow relaxation of magnetization in zero-field for a Co(II) triimidosulfonate complex (**C**),[11f] and later the groups of Sarkar and van Slageren reported a Co(II) bis(sulfonamido)benzene complex that exhibits hysteresis at 1.8 K with coercivity at a sweep rate of 500 Oe s$^{-1}$ (**E**).[11h] Recently the influence of the N–Co–N bite angle in four-coordinate Co(II) triimidosulfonate complexes[11g] (**C** in Chart 1) and Co(II) bis(methanesulfonyl)oxamidate complexes[11i] (**D** in Chart 1) has been elucidated, and bite angles around 76–78° and 81°, respectively, were found to be ideal for harnessing large ZFS. The Plass group has investigated different solvates of pseudo-tetrahedral bis-chelate {$N_2O_2$} Co(II) SIMs and concluded that the spin-reversal barrier increases with stronger distortion away from the tetrahedral toward a square-planar geometry; in the studied solvomorphs the dihedral twist angles between the N–Co–O chelate planes of the two Schiff-base ligands varied between 86° and 55.9°, with $D$ values in the range from −25 to −40 cm$^{-1}$.[20]

In the present work, we report a family of tetracoordinate dianionic cobalt(II) complexes of the general formula $[^{F}L_2Co]X_2$ where $^{F}L$ is a bidentate *N*,*N*′-bis(perfluorophenyl)oxalamido ligand, and X are different cations. While metal amido bonds

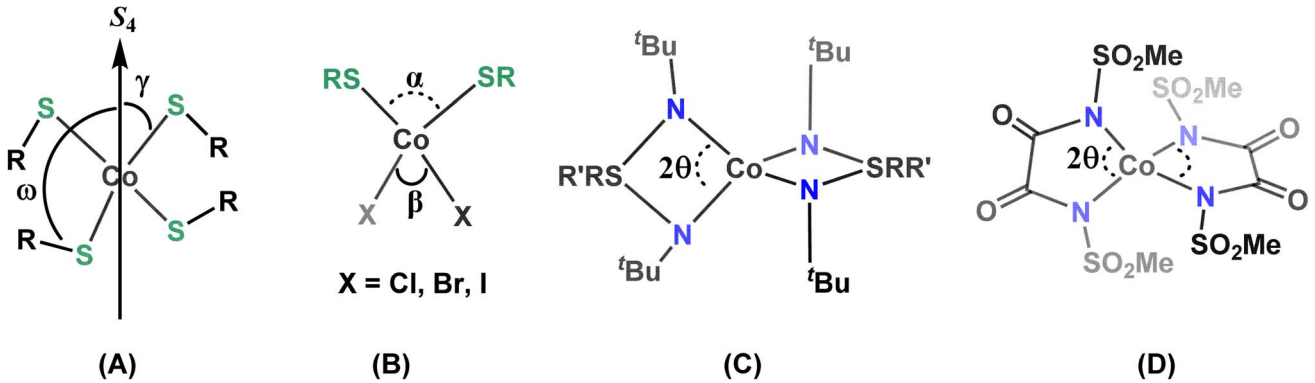


Chart 1 Selected examples of magneto-structural correlations (A–D) studied for four-coordinate Co(II) SIMs.

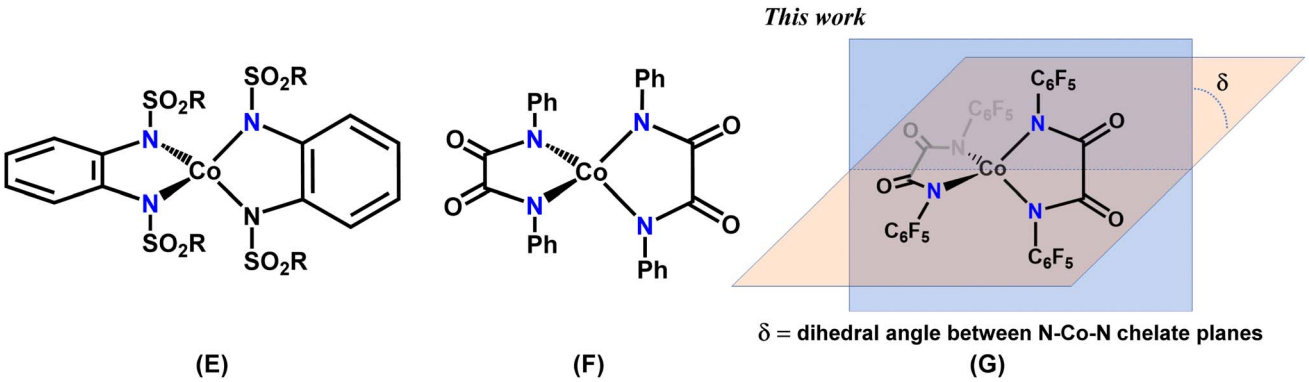


Chart 2 Examples of homoleptic dianionic four-coordinate Co(II) SIMs (E–G).

tend to be susceptible to hydrolysis, the strongly electron-withdrawing $C_6F_5$ substituents on the coordinating amido nitrogen atoms impart ambient air and moisture stability. Variation of the non-coordinating cations leads to very different dihedral twist angles ($\delta$) of the N–Co–N coordination planes (**G** in Chart 2) in the solid state, which is shown to translate into significant alterations of the magnetic properties. We present a combined experimental and theoretical study on this set of complexes in order to unravel the magneto-structural correlations and to decipher and benchmark the factors that lead to the dihedral angle dependence of the magnetic properties.

## Results and discussion

### Synthesis and structural characterization

The diamido ligand, *N*,*N*′-bis(perfluorophenyl)oxalamide ($^{F}LH_2$) was synthesized using a reported literature procedure.[21] The $-C_6F_5$ substituent was chosen to decrease the net charge density on the coordinating amido nitrogen atom, translating into a decreased ligand field strength. Additionally, this improves the robustness of the metal-amido bonds which are usually known to be susceptible to hydrolysis (*vide infra*). The mononuclear cobalt complexes were readily synthesized by the reaction of the dipotassium salt of the ligand in dry THF and anhydrous $CoCl_2$ in a molar ratio of 2 : 1 under an inert atmosphere (Scheme 1). Cation exchange with tetrabutylammonium (TBA) bromide and tetraphenylphosphonium bromide introduced different non-coordinating counterions and allowed for the isolation of $[^{F}L_2Co](TBA)_2$ (**1**) and $[^{F}L_2Co](PPh_4)_2$ (**2**), respectively. To further understand the effect of the charge-balancing cations on the magnetic properties, 18-crown-6 ether was directly added to the reaction mixture to isolate $[^{F}L_2Co(K@18\text{-crown-}6)_2]\cdot 2Et_2O$ (**3**), where the $K^+$ ions are hosted in the crown ether but additionally coordinated by the carbonyl oxygen atoms of the oxalamide ligands.

The iso-structural zinc(II) complexes $[^{F}L_2Zn](TBA)_2$ (**4**), $[^{F}L_2Zn](PPh_4)_2$ (**5**), and $[^{F}L_2Zn(K@18\text{-crown-}6)_2]\cdot 2Et_2O$ (**6**) were prepared using a similar synthetic procedure. All the complexes were found to be stable under ambient aerobic conditions, both in the solid state and solution phase. All six complexes were

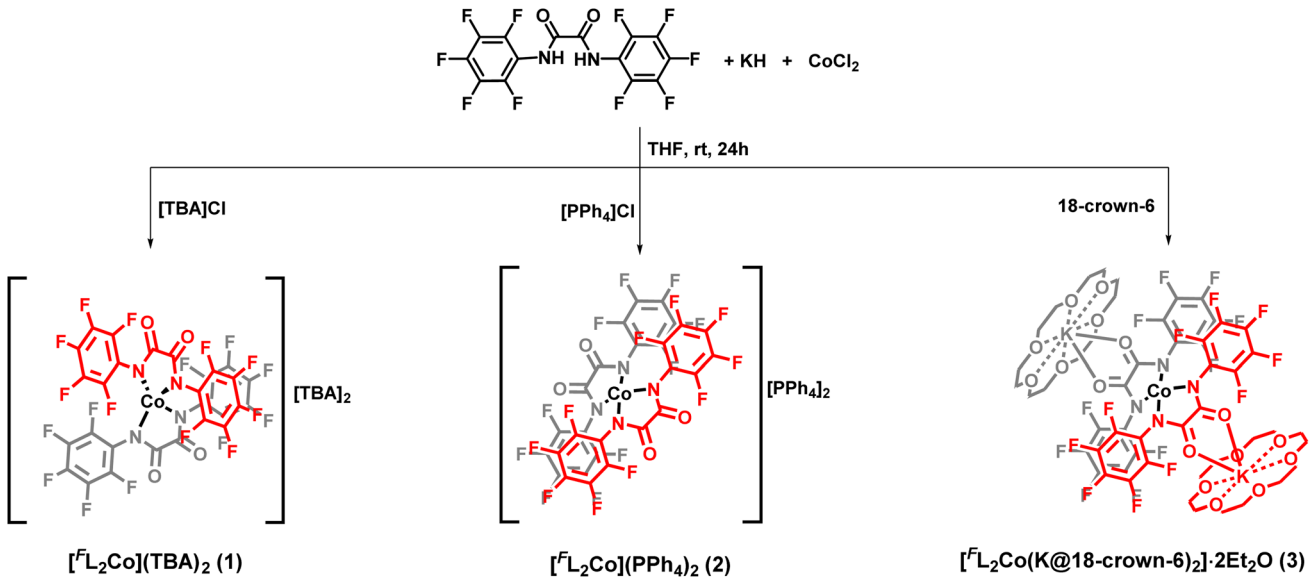


Scheme 1 Syntheses of the tetracoordinate Co(II) complexes **1**–**3**.

characterized by several analytical and spectroscopic techniques as well as by elemental analysis (see below and ESI for details†). Cyclic voltammetry (CV) was measured for **1–3** in MeCN solution. The complexes exhibit an irreversible first oxidation at anodic peak potentials $E_a^p = +0.09$ V (**1**, **2**) or +0.05 V (**3**; all at 100 mV $s^{-1}$; *vs.* the $Fc^+/Fc$ couple; Fig. S23–S25†). These values are significantly higher by 0.31 or 0.27 V, respectively, compared to the irreversible first oxidation at $E_a^p = -0.22$ V (Fig. S26†) recorded under the same conditions for a related complex $[^{Cl}L_2Co](TBA)_2$ (**H**)[11g] that has less electron withdrawing 4-chlorophenyl substituents in the ligand $[^{Cl}L]^{2-}$ instead of the pentafluorophenyl substituent in $[^{F}L]^{2-}$. These findings are in line with the observed robustness of **1–3** under ambient conditions.

Solutions of these compounds appear orange in different solvents and solid compounds **2** and **3** are also orange, but complex **1** was isolated as a magenta solid. Attempts to grow crystals of complex **1** from different solvents, either by slow diffusion of diethyl ether into the orange solutions or by cooling, always resulted in the isolation of magenta crystals. Block-shaped orange single crystals of complex **2** as well as block-shaped orange-yellow crystals of **3** were obtained by slow diffusion of diethyl ether into DMF solutions. X-ray diffraction analyses revealed the molecular structures of the anions $[^{F}L_2Co]^{2-}$ as shown in Fig. 1 ($[^{F}L_2Co(K@18C6)_2]$ in case of **3**).

Complex **1** crystallizes in the monoclinic space group *P*2/*c* with four crystallographically independent molecules in the asymmetric part of the unit cell (**1a–1d**). The Co(II) ions are coordinated by two orthogonally oriented dianionic ligands $[^{F}L]^{2-}$ (Fig. 1, S27 and S28†) with average Co–N bond lengths of 1.992 Å, the charge being balanced by TBA cations in the crystal lattice. The N–Co–N bite angles from the bidentate oxanilido ligands (av. 81.2°) are considerably smaller than the other N–Co–N angles (av. 124.8°) leading to an approximate $D_{2d}$ symmetry or elongated tetrahedron ($\tau_4$ = 0.65–0.78).[22] The relatively small ligand bite angle is quite close to the value of 76–78° recently proposed as an ideal bite angle for inducing large axial zero-field splitting in $\{N_4\}$-ligated Co(II) complexes.[11g] The dihedral angle $\delta$ between the N–Co–N chelate planes ranges from 72.6 to 89.2° for the four molecules in the unit cell (average 83.08°). A continuous shape measure (CSM) analysis of the local coordination environment of the Co(II) ions reveals significant deviation from an ideal tetrahedral geometry (see Table S3†). The nearest Co(II) ions are separated by a minimum distance of 11.43 Å in the lattice due to the presence of the bulky charge-balancing TBA cations.

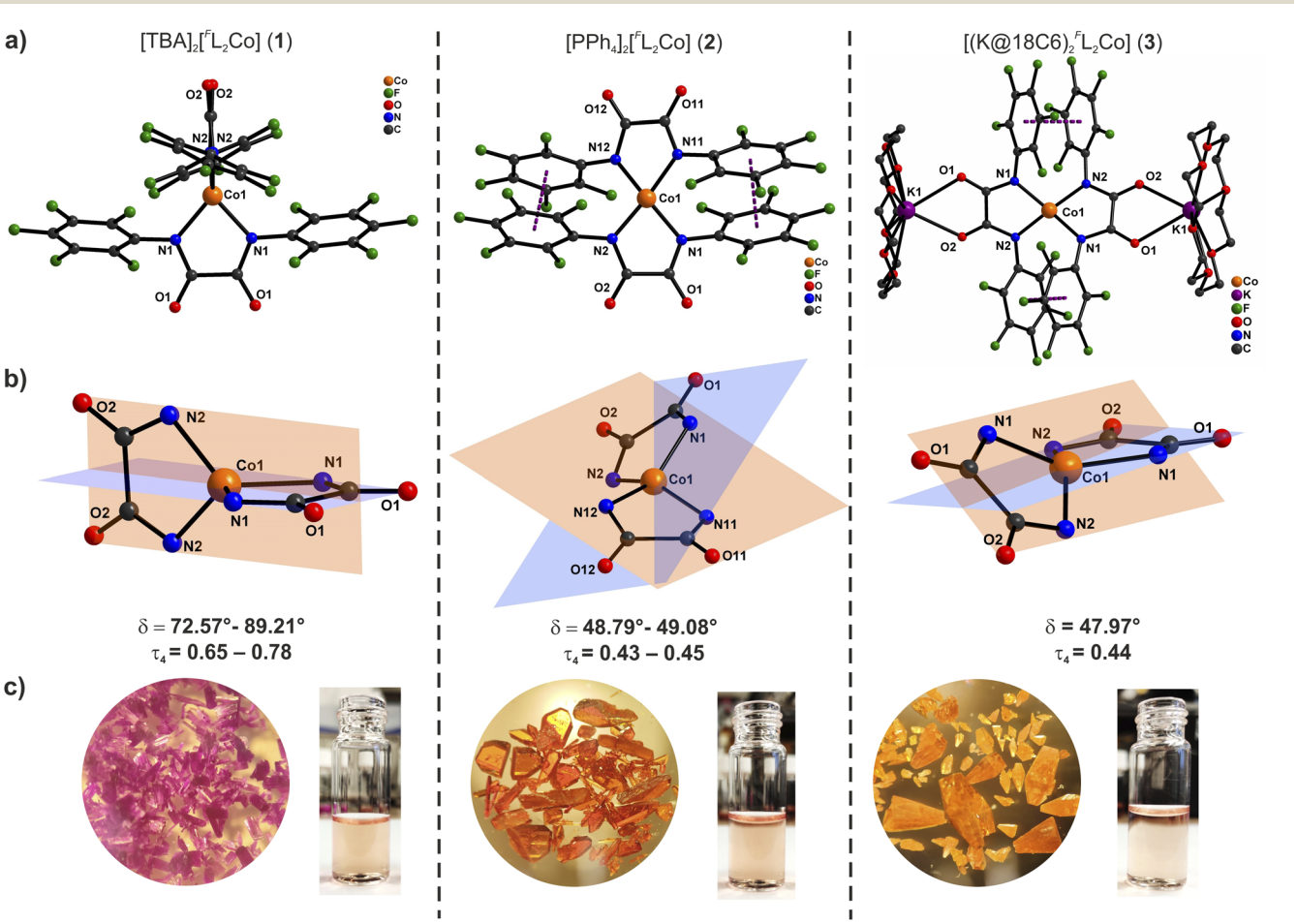


Fig. 1 (a) Molecular structures of the anions of **1** (left) and **2** (middle), and **3** (right); cations have been omitted for clarity in case of **1** and **2**. (b) Core structures of **1–3** showing the two intersecting N–Co–N chelate planes. (c) Complexes **1–3** in the solid state and DMF solution.

Complex **2** crystallizes in the triclinic space group $P\bar{1}$ where the asymmetric part of the unit cell contains one and a half molecules of $[^{F}L_2Co]^{2-}$ and three tetraphenylphosphonium cations. The Co(II) ions are found in a distorted seesaw coordination environment (Fig. 1, S29 and S30†) with an average Co–N bond length of 1.985 Å. The entire ligand system is disordered over two positions, but overall the anions are structurally similar and roughly superimposable (Fig. S30d†); no disorder was observed for any of the tetraphenylphosphonium cations. The average N–Co–N bite angles from the bidentate oxanilido ligands (82.4°) are comparable to those of **1**, but the other four N–Co–N angles show a wider range (104.4–154.6°), reflecting the distorted seesaw coordination sphere of the Co(II) ions (approximate $D_2$ symmetry with $\tau_4 = 0.43$–$0.45$, Table S3†). The average dihedral twist angle $\delta$ between the N–Co–N chelate planes is 48.56°. The electron-deficient aryl rings appear to be involved in π–π interactions with distances between adjacent centroids in the range 3.41–3.73 Å. Nearest Co(II) ions within the lattice are separated by more than 10 Å.

Complex **3** crystallizes in the monoclinic space group $C2/c$, and the structural features of its $[^{F}L_2Co]^{2-}$ core are very similar to those of **2**. The asymmetric part of the unit cell contains half of a molecule with the Co(II) ion in a distorted seesaw coordination environment (Fig. 1, S31 and S32†). The $K^+$ ions are hosted in the 18-crown-6 macrocycle and are additionally coordinated by the amide oxygen atoms of the $[^{F}L]^{2-}$ ligands. In this case, and in contrast to **2**, the ligands in **3** are not disordered, likely due to the steric constraints imposed by the 18-crown-6 moiety on the free rotation of the $-C_6F_5$ groups. The average Co–N bond length is 1.982 Å and the average N–Co–N bite angle is 82.8°. The average dihedral angle $\delta$ between the N–Co–N chelate planes is 48.0°, similar to the situation in **2** (approximate $D_2$ symmetry with $\tau_4 = 0.44$, Table S3†). As observed for complex **2**, the aryl rings are involved in π–π interactions with a distance of 3.531 Å between the nearest ring centroids. The nearest Co(II) neighbors are separated by a distance of more than 12 Å in the lattice.

### Experimental absorption spectra

Solutions of all three complexes **1–3** in DMF or MeCN appear similar in color (Fig. S19†), and their UV-Vis-NIR spectra are almost identical (Fig. S19 and S20†); they exhibit three distinct absorption bands around 17 600 $cm^{-1}$, 9700 $cm^{-1}$, and 8500 $cm^{-1}$ with similar molar extinction coefficients (Fig. S19 and S20†). This observation indicates that although complexes **1–3** adopt different structures in solid-state, in solution the anions $[^{F}L_2Co]^{2-}$ are essentially identical and independent of the type of cation ($NBu_4^+$ in **1**, $PPh_4^+$ in **2**, $[K@18\text{-crown-6}]^+$ in **3**). In the range 7100–12 500 $cm^{-1}$ the solution spectra of **1–3** are similar to the solid-state spectra of **2** and **3** (*vide infra*) with a characteristic double-humped band peaking around 9600 $cm^{-1}$ and 8500 $cm^{-1}$. However, the relatively sharp and intense band at 17 600 $cm^{-1}$ with its high-energy shoulder (Fig. S19†) is more reminiscent of the absorption feature observed for solid **1** (*vide infra*). This suggests that in solution the complexes might be present in a conformation with a dihedral twist angle $\delta$ in between those found for **1** *vs.* **2** (or **3**) in solid-state.

### Static magnetic properties of solid compounds

Magnetic studies for complexes **1–3** were performed on polycrystalline powdered samples packed in a polycarbonate capsule. The powdered samples were covered with low-viscosity perfluoropolyether-based inert oil Fomblin Y45 to prevent any torquing. The $\chi_M T$ value of 3.34 $cm^3$ K $mol^{-1}$ for complex **1** at 210 K is larger than the expected spin-only value of one isolated Co(II) ion (1.875 $cm^3$ K $mol^{-1}$ for $S = 3/2$ and $g = 2.0$), suggesting a significant orbital contribution to the observed magnetic moment. The $\chi_M T$ value decreases gradually upon lowering the temperature and falls sharply below 8 K, reaching a value of 2.50 $cm^3$ K $mol^{-1}$ at 2 K (Fig. 2a). Since the nearest Co(II) centres are separated by a distance of 11.43 Å in the crystal lattice and significant intermolecular interactions are thus unlikely, the sharp fall of $\chi_M T$ at lower temperatures can be associated with

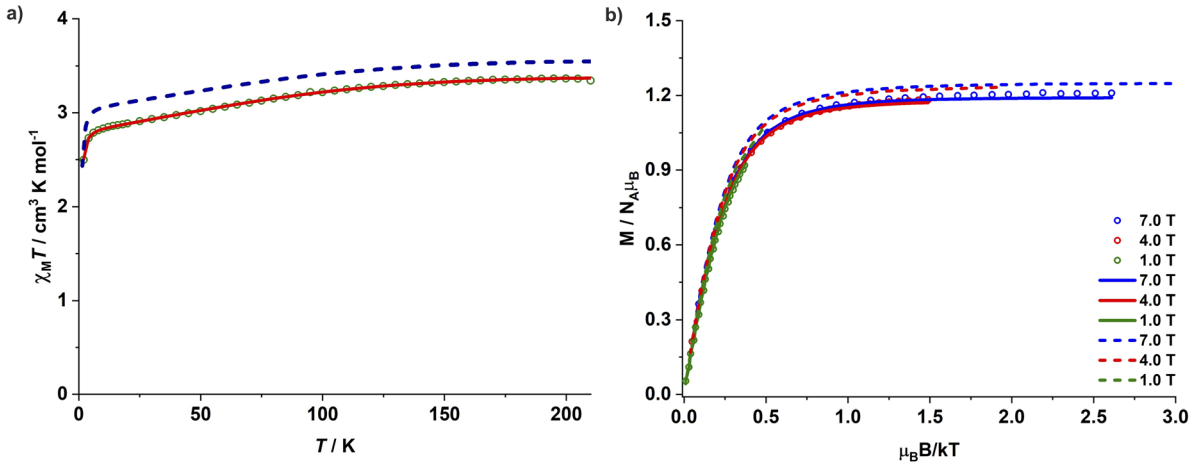


Fig. 2 (a) Variable-temperature $\chi_M T$ product for complex **1** measured under an applied DC field of 0.5 T. (b) Variable-temperature variable-field magnetization for complex **1**. The solid lines are the best fit with $D = -143$ $cm^{-1}$, $g_x = g_y = 2.25$, and $g_z = 3.15$ and the dashed lines are the theoretical predictions with CASSCF/NEVPT2.

Table 1 Summary of the structural features and the various magnetic parameters determined experimentally and obtained by CASSCF/NEVPT2

| | | Experiment | | | | | Theory (NEVPT2) | | | | | |
|---|---|---|---|---|---|---|---|---|---|---|---|---|
| Complex | $\delta$ (°) | $g_x$ | $g_y$ | $g_z$ | $D$ (cm$^{-1}$) | $E/D$ | $g_x$ | $g_y$ | $g_z$ | $D$ (cm$^{-1}$) | $E/D$ | $E(^4B_2)$ (cm$^{-1}$) |
| **1a** | 88.2 | 2.25 | 2.25 | 3.15 | −143 | 0 | 1.50 | 1.51 | 3.53 | −149.7 | 0.001 | 94 |
| **1b** | 89.2 | | | | | | 1.52 | 1.53 | 3.52 | −149.2 | 0.001 | 100 |
| **1c** | 82.3 | | | | | | 1.58 | 1.61 | 3.51 | −147.4 | 0.002 | 134 |
| **1d** | 72.6 | | | | | | 1.65 | 1.74 | 3.48 | −142.7 | 0.007 | 186 |
| **2a** | 48.8 | 2.37 | 2.37 | 2.85 | −75 | 0.067 | 1.99 | 2.20 | 2.97 | −73.8 | 0.082 | 928 |
| **2b** | 49.1 | | | | | | 2.00 | 2.19 | 2.95 | −73.1 | 0.072 | 1013 |
| **3** | 48.0 | 2.36 | 2.36 | 2.77 | −69 | 0.072 | 1.98 | 2.20 | 3.01 | −77.9 | 0.081 | 856 |

the presence of ZFS and large magnetic anisotropy. The magnetization for **1** increases linearly until 1 T at 2 K and more gradually above 2 T. It reaches a value of 2.4 $\mu_B$ at 7 T, however, without any complete saturation (Fig. S37†) and well below the expected $M_{sat}$ value of 3.0 $\mu_B$ for an isolated isotropic Co(II) ion ($S = 3/2$). Simultaneous fitting of the magnetic susceptibility data along with the variable-temperature variable-field (VTVH) magnetization data with the program julX_2S[23] (see details in ESI†) yields the best fit with $D = -143$ cm$^{-1}$ and $g_x = g_y = 2.25$ and $g_z = 3.15$ (Fig. 2b). This translates into a large energy separation of *ca.* 286 cm$^{-1}$ (411 K, $2D$) between the well-isolated ground $M_S = \pm 3/2$ Kramers doublet (KD) and the excited state $M_S = \pm 1/2$ KD. The $\chi_M T$ values for **2** and **3** are 3.09 and 3.00 cm$^3$ K mol$^{-1}$ at 210 K, and 2.10 and 1.99 cm$^3$ K mol$^{-1}$ at 2 K, respectively (Fig. S38 and S41†). The corresponding simultaneous fit of the magnetic susceptibility and VTVH magnetization data yields a high negative ZFS parameter $D$ along with a significant rhombic component $E$. The best fit parameters obtained are $D = -75$ cm$^{-1}$, $E/D = 0.067$ and $g_x = g_y = 2.37$ and $g_z = 2.85$ for **2** (Fig. S38 and S39†) and $D = -69$ cm$^{-1}$, $E/D = 0.072$ and $g_x = g_y = 2.36$ and $g_z = 2.79$ for **3** (Fig. S41 and S42†), respectively. Table 1 summarizes the structural features of **1–3** and the various magnetic parameters determined experimentally by SQUID magnetometry.

### Dynamic magnetic properties of solid compounds

To gain insights into the magnetic relaxation dynamics, ac susceptibility measurements were carried out for complex **1** in the frequency range 0.1–1000 Hz at zero DC field. A clear frequency dependence of the maxima in the out-of-phase ($\chi''_M$) components of the ac susceptibility is observed (Fig. 3 and S44†). The relaxation times were extracted by fitting the in-phase ($\chi'_M$) and out-of-phase ($\chi''_M$) components of the ac susceptibility to a generalized Debye model using the CC-FIT2 program.[24] The temperature dependence of the relaxation time was modelled by considering various potential relaxation pathways using eqn (1)

$$1/\tau = 1/\tau_{QTM} + CT^n + \tau_0^{-1}\exp(-U_{eff}/k_BT) \quad (1)$$

where the terms correspond to relaxation *via* quantum tunnelling, the Raman process, and the Orbach relaxation pathway, respectively. The least number of parameters was used in all cases to avoid overparameterization (see ESI for details†). However, no satisfactory fit for **1** was obtained for the relaxation rates with any combination of these relaxation processes, as previously observed in the case of many Co(II) SIMs.[9b,11h,q,13a,25] It should be noted that the asymmetric part of the unit cell for solid complex **1** contains four crystallographically independent molecules with a significant variation in dihedral angles (72.6 to 89.2°), which significantly affects the slow relaxation dynamics and magnetic properties (*vide infra*). Thus, the relaxation time ($\tau$) extracted has contributions from all four crystallographically independent molecules. In addition, some complex relaxation mechanisms may be operative at lower temperatures. However, by restraining $U_{eff}$ to $2D$ as in previously reported studies for

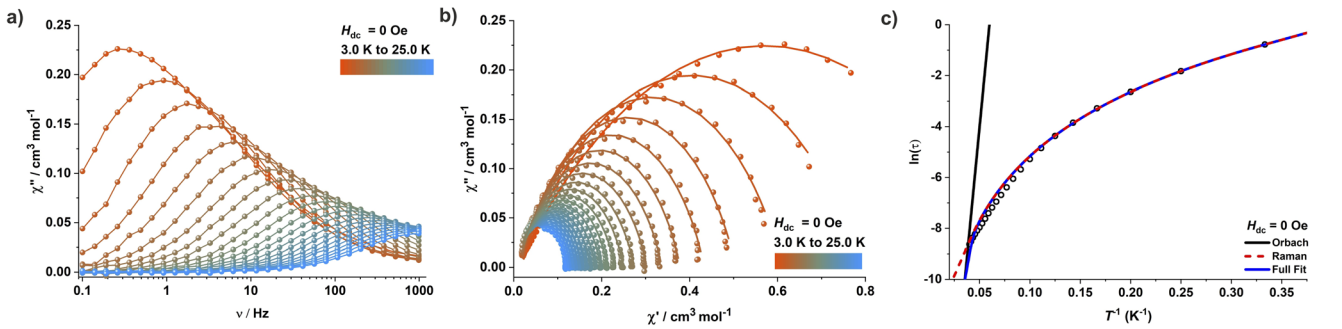


Fig. 3 (a) Out-of-phase ($\chi''_M$) component of the frequency-dependent (0.1–1000 Hz) AC susceptibility for **1** measured in an oscillating AC field of 3.0 Oe under zero DC field. (b) Cole–Cole plots for **1** under zero DC field. (c) Dependence of the natural logarithm of the relaxation time ln($\tau$) on inverse temperature ($T^{-1}$); the solid blue line represents the best fit considering a combination of Orbach ($U_{eff} = 410$ K, $\tau_0 = 2.25 \times 10^{-11}$ s) and Raman ($C = 0.0399$ s$^{-1}$ K$^{-n}$, $n = 3.64$) relaxation pathways.

highly anisotropic Co(II) SIMs[11h,q,13a] and fixing its value to 410 K, a reasonable curvature of the temperature dependence of the relaxation rate could be obtained ($U_{eff}$ = 410 K, $\tau_0 = 2.25 \times 10^{-11}$ s, $n = 3.64$ and $C = 0.0399\ s^{-1}\ K^{-n}$), albeit still deviating slightly in the higher temperature range (Fig. 3c). Hence, we refrain from analyzing the fits for complex **1** in greater detail. The relaxation rate simulated based on the Raman process is almost congruent with the curve derived from Raman and Orbach processes, except for the high temperature regime. A fit considering only the Raman process yields $C = 0.0319\ s^{-1}\ K^{-n}$, $n = 3.80$ (Fig. S44e†), and relaxation of **1** over the entire temperature range seems to be dominated by the Raman process, with the Orbach process being relevant at higher temperatures. Application of an optimum DC field of 3000 Oe had only a slight effect on the slow relaxation dynamics, however, it slightly slowed down the relaxation at lower temperatures, indicating that quantum tunneling still is a contributing factor in the magnetic relaxation dynamics albeit to a lesser extent (Fig. S45†). In order to further understand the relevance of dipolar effects or QTM, AC susceptibility measurements were performed on a magnetically diluted sample **1′** (*ca.* 10% **1** in the analogous zinc(II) complex **4**), and a reasonable AC susceptibility signal could be obtained (Fig. S48†). Analysis of the data reveals that the dilution only marginally affects the relaxation dynamics in the low-temperature regime, thus indicating that the origin of the slow relaxation of magnetization is indeed molecular in nature. Yet a linear temperature dependence at the highest temperatures is still absent. Nevertheless, the relaxation times are slightly slower for the diluted sample **1′** as compared to pure **1** (Fig. S49†).

The large energy separation between the ground state ($M_S = \pm 3/2$) and excited state ($M_S = \pm 1/2$) KD also prompted us to carry out magnetic hysteresis experiments. Variable-field magnetization data measured at a modest sweep rate of 30 Oe $s^{-1}$ revealed a waist-restricted hysteresis loop up to 3.5 K with a non-negligible coercivity of ~100 Oe at 1.8 K (Fig. 4a). The sharper magnetization decay towards zero field is most probably due to QTM between the low-lying KDs. These characteristic features are quite common among Co(II) SIMs and have also been observed in recently reported two and four-coordinate Co(II) based SIMs featuring very high energy barriers.[9,11h,q] The opening of the hysteresis loops becomes more apparent in the magnetically diluted material, with the coercivity increasing to ~300 Oe at 1.8 K for a sample with *ca.* 2% **1** in **4** (**1″**) (Fig. 4b). Magnetic blocking is also evident from the divergence of the zero-field cooled (ZFC) – field cooled (FC) variable temperature magnetization measurements. The maxima in the ZFC curve is at 3.5 K, whereas the divergence of the ZFC–FC variable temperature magnetization starts above 4.0 K (Fig. 4c). The combination of these properties with its ruggedness under ambient conditions makes this Co(II) complex **1** one of the best-performing 3d-SIMs.

Interestingly, complexes **2** and **3** show dramatically different magnetic properties compared to **1**, since both do not exhibit any maxima in the out-of-phase ($\chi''_M$) AC susceptibility signals under zero applied DC field (Fig. S54 and S56†). While complex **3** features only very weak positive $\chi''_M$ signals at very low temperatures, $\chi''_M$ signals are completely absent in case of complex **2**. These observations are not unexpected given the large rhombic ZFS parameter ($E$) derived from the DC susceptibility measurements, which is known to lead to undercutting of the over-barrier relaxation pathway *via* QTM. Application of an optimum DC field of 2000 Oe and 3000 Oe, respectively, led to the observation of well-resolved frequency-dependent $\chi''_M$ maxima in the AC susceptibility measurements of **2** (Fig. 5 and S55†) and **3** (Fig. S57†). Relaxation times were extracted by fitting the AC susceptibility data with a generalized Debye model; relaxation was found to be dominated by QTM and Raman pathways. The best-fit parameters obtained are $C = 0.473\ s^{-1}\ K^{-n}$ and $n = 5.02$ (Raman) for **2** (Fig. 5c). Complex **3** exhibits similar relaxation dynamics (Fig. S57†), suggesting that the binding of charge-balancing cations to the ligand periphery (K@18C6 in **3**) does not significantly influence the slow relaxation dynamics if the core coordination environment of the central paramagnetic ion, including the dihedral angle, is comparable.

In contrast to pristine undiluted material of **2** and **3**, magnetically diluted samples containing *ca.* 10% **2** or **3** in the corresponding zinc(II) compounds **5** or **6** (called **2′** and **3′**, respectively) exhibit slow relaxation dynamics even in zero DC field, although only below 6 K (Fig. S58†) or 8 K (Fig. S61†). This might be due to the suppression of dipolar exchange interactions in the diluted samples, which may result in additional quantum tunnelling pathways. These findings suggest that

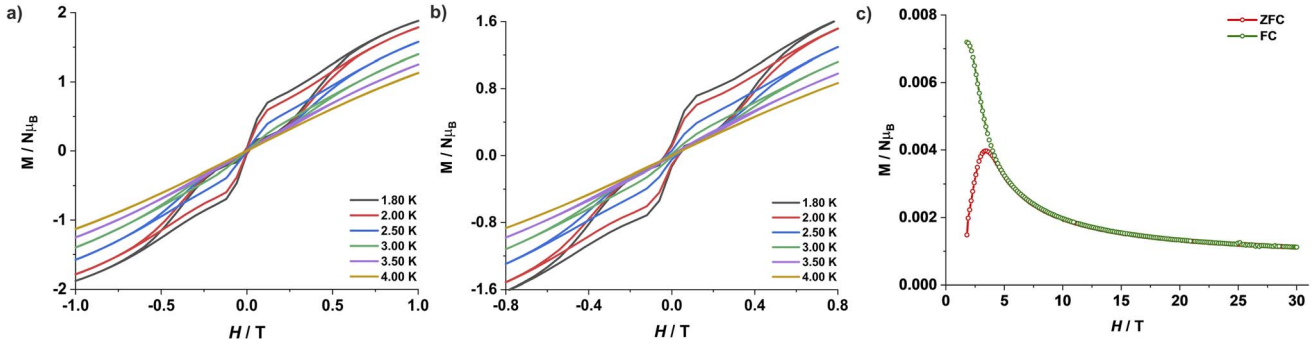


Fig. 4 Variable field magnetization for (a) **1** and (b) **1″** at a sweep rate of 30 Oe $s^{-1}$ at indicated temperatures. (c) The plot of the zero field-cooled (red) and field-cooled (green) magnetization *vs.* temperature for **1″** at an applied field of 50 Oe and a sweep rate of 2 K $min^{-1}$.

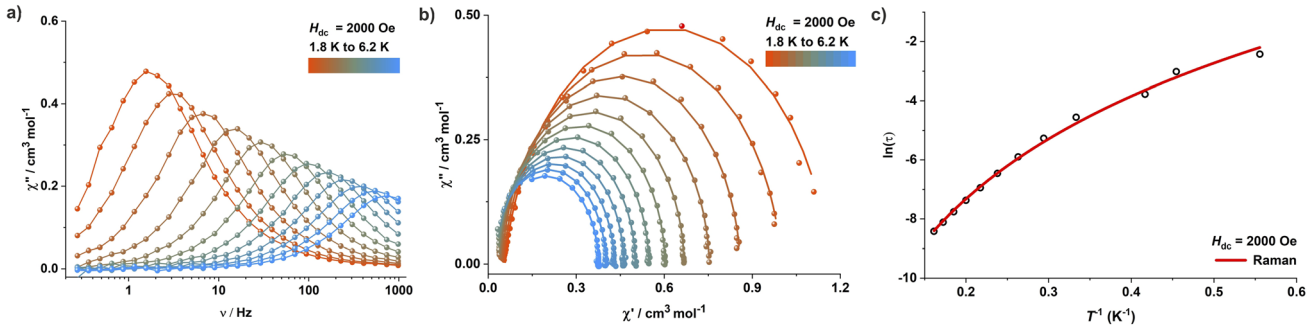


Fig. 5 (a) Out-of-phase ($\chi''_M$) component of the frequency-dependent (0.1–1000 Hz) AC susceptibility measured in an oscillating AC field of 3.0 Oe under an applied DC field of 2000 Oe for complex **2**. (b) Cole–Cole plots for **2** under an applied DC field of 2000 Oe. (c) Dependence of the natural logarithm of the relaxation time ln($\tau$) on inverse temperature ($T^{-1}$); the solid red line represents the best fit considering a Raman ($C = 0.473$ s$^{-1}$ K$^{-n}$, $n = 5.02$) relaxation pathway.

dipolar exchange coupling interactions can affect the slow relaxation dynamics even if the paramagnetic metal ions are more than 10 Å apart in the crystal lattice. QTM dominates the slow relaxation dynamics at lower temperatures for both **2′** and **3′**, while the Raman process dominates at higher temperatures. The application of a DC field of 2000 Oe suppresses any QTM at lower temperatures in **2′** and **3′**, which then show slow relaxation dynamics comparable with those observed for **2** and **3**, respectively, under an applied DC field (Fig. S59 and S62†). Magnetic hysteresis experiments were performed on magnetically diluted samples containing *ca.* 2% **2** or **3** in the zinc(II) compound **5** or **6**, respectively, *viz.* **2″** (Fig. S60†) and **3″** (Fig. S63†), but magnetic hysteresis could not be observed in either case.

### Magnetic properties in frozen solution

The obvious differences in color and UV-Vis-NIR spectral properties between the solid samples and dissolved complexes prompted us to measure the static and dynamic susceptibilities of the complexes in frozen solutions. A reasonable signal-to-noise ratio could be obtained for 0.12 M DMF solutions of complexes **1** and **2** (solubility in MeCN is too limited); the experiment could not be performed for complex **3** due to the low solubility of the complex. The best fit of the magnetic susceptibility data along with the variable-field variable-temperature (VTVH) magnetization yields $D = -78$ cm$^{-1}$, $g_x = g_y = 2.16$ and $g_z = 2.87$ for **1** (Fig. 6, S64 and S65†) and $D = -72$ cm$^{-1}$, $g_x = g_y = 2.22$ and $g_z = 2.72$ for **2**, respectively (Fig. S69 and S70†). The frozen DMF solutions of **1** and **2** display comparable slow relaxation dynamics under zero DC field with QTM dominating the slow relaxation process at lower temperatures (Fig. 6). The relaxation times extracted could be fitted assuming a combination of QTM and Raman relaxation mechanisms (Fig. 6c, S66d, and S71d†). Application of a DC field substantially suppresses the dominating QTM at low temperatures for the frozen DMF solutions of **1** and **2**, which again display comparable slow relaxation dynamics (Fig. S67 and S72†); relaxation times over the entire temperature range could be fitted with a combination of Raman and QTM processes (Fig. S67d and S72d†). Parameters for the relaxation dynamics of **1** and **2** in frozen DMF solution are also similar to the ones observed for solids **2** and **3**. These combined UV-Vis-NIR spectral and magnetic properties indicate that although complexes **1** and **2**/**3** exist in different structural forms in the solid state, their anions $[^{F}L_2Co]^{2-}$ adopt identical structures in solution, likely close to the ones found

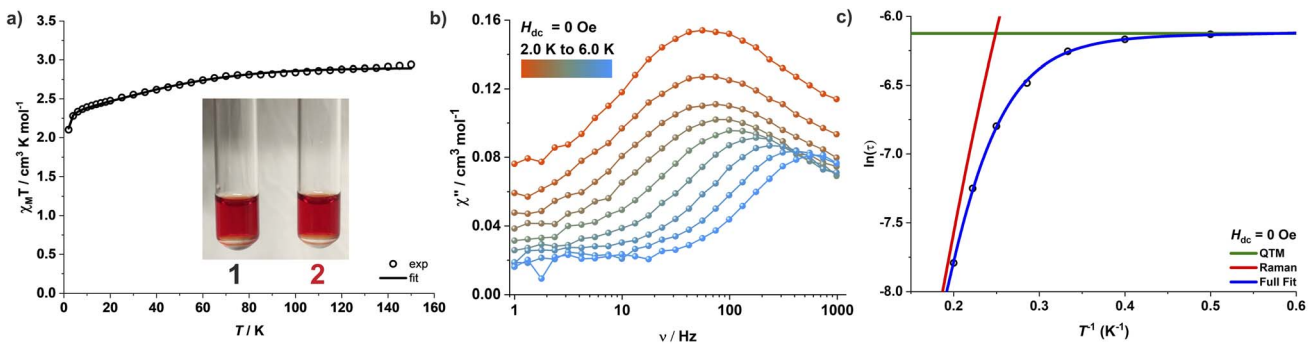


Fig. 6 (a) Variable-temperature $\chi_M T$ product for a frozen DMF solution of **1** measured under an applied DC field of 0.5 T. Inset: DMF solution of complex **1** and **2** in a sealed NMR tube. (b) Out-of-phase ($\chi''_M$) component of the frequency-dependent (0.1–1000 Hz) AC susceptibility in an oscillating AC field of 3.0 Oe for a frozen DMF solution of **1** under zero DC field. (c) Dependence of the natural logarithm of the relaxation time ln($\tau$) on inverse temperature ($T^{-1}$); the solid blue line represents the best fit considering a combination of Raman ($C = 0.047$ s$^{-1}$ K$^{-n}$, $n = 6.61$), and QTM ($\tau_{QTM} = 2.19 \times 10^{-3}$ s) relaxation pathways.

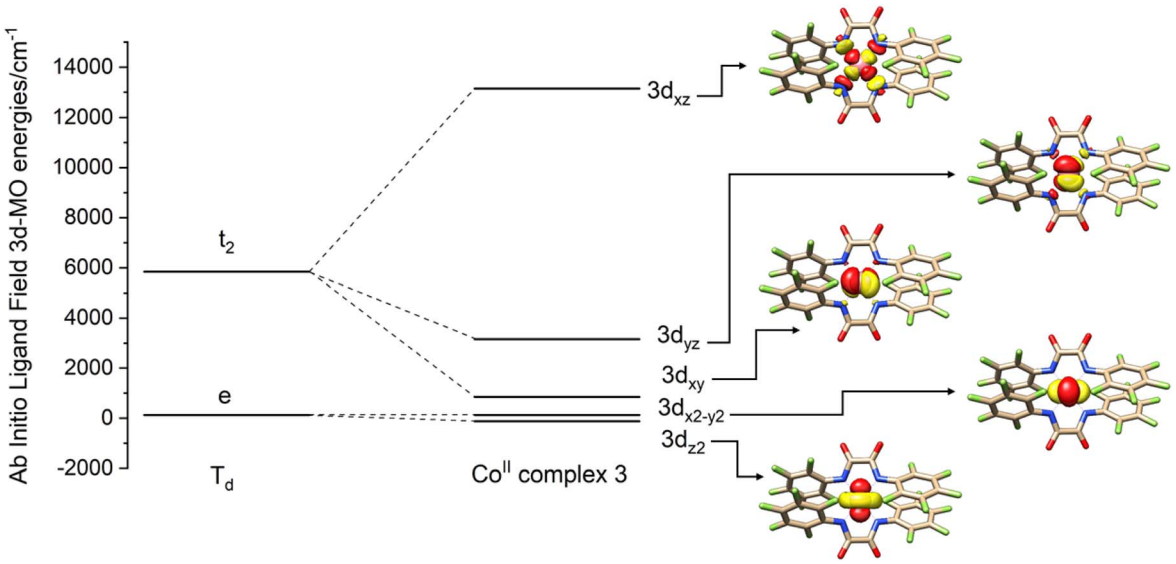


Fig. 7 AILFT molecular orbital diagram for complex **3** at the NEVPT2 level. The geometry is determined crystallographically. Orbital images are shown on the right. While the orbital ordering is generally preserved across the complexes, the gap between $3d_{xy}$ and $3d_{x^2-y^2}$ orbitals is reduced in complex **1**.

for crystalline **2** and **3**. It is interesting to note that while no hysteresis was observed in the magnetically diluted solid samples **2**″ and **3**″, the frozen solutions of **1** and **2** display magnetic hysteresis at 1.8 K, although without coercivity (Fig. S68 and S73†).

### Computed electronic structure

Since **1–3** show identical UV-Vis-NIR spectra in solution while packing in the crystal lattice seems to distort the complex from this ideal geometry, structures were not computationally optimized but calculations were based on coordinates obtained from the X-ray crystallographic structure determinations. In the presence of several disordered forms of the anion $[^{F}L_2Co]^{2-}$, all the structures were analyzed (**1a–d**; **2a,b**). Computations were carried out with the ORCA package,[26] and the spectrum of the Hamiltonian was computed using the state averaged complete active space self-consistent field method (SA-CASSCF)[27] with n-electron valence perturbation theory to second-order (NEVPT-2).[28] Further details are provided below and in the ESI.†

In Fig. 7, the molecular orbital energies of complex **3** are compared to the energies of an idealized tetrahedral complex. The lowest energy MOs are in order: $d_{z^2}$, $d_{x^2-y^2}$, $d_{xy}$, $d_{yz}$, $d_{xz}$. As expected, the e orbitals are lower in energy than the $t_2$ orbitals. The electronic structure of the quartets in an ideal $T_d$ geometry is in the order $^4A_2(F) < {}^4T_2(F) < {}^4T_1(F) < {}^4T_1(P)$. Upon reduction of the symmetry from $T_d$ to $D_{2d}$, the $^4A_2$ state reduces to $^4B_1$ while $^4T_2$ splits into a $^4B_2$ and a $^4E$ state, and the $^4T_1$ splits into a $^4A_2$ and a $^4E$ state. Computations yield the ordering of energies in the $D_{2d}$ point group according to $^4B_1 < {}^4B_2 < {}^4E < {}^4A_2 < {}^4E < {}^4A_2 < {}^4E$. Further crystal distortions lift the degeneracy of the $^4E$ state in the CASSCF/NEVPT2 calculations. A comparison of scalar relativistic energies obtained at the NEVPT2 level with the spin-allowed transitions deduced from optical absorption

Table 2 Comparison of experimental energies obtained from Gaussian deconvolution of UV-Vis-NIR spectrum using orca_asa module and theoretical energies obtained at the NEVPT2 level. Excitations are from the ground state $^4B_1$ ($D_{2d}$ point group) originating from the $^4A_2$ from the parent $T_d$ point group

| Point group | Experimental energies ($cm^{-1}$) | | | Point group | NEVPT2 energies ($cm^{-1}$) | | | | | | |
|---|---|---|---|---|---|---|---|---|---|---|---|
| $T_d$ | **1** | **2** | **3** | $D_{2d}$ | **1a** | **1b** | **1c** | **1d** | **2a** | **2b** | **3** |
| $^4T_2(F)$ | — | — | — | $^4B_2$ | 76 | 80 | 115 | 172 | 928 | 1013 | 856 |
| | | | | $^4E$ | 8733 | 8628 | 7789 | 6311 | 4191 | 4103 | 4008 |
| | | | | | 8882 | 8744 | 8384 | 7315 | 6432 | 6536 | 6148 |
| $^4T_1(F)$ | 8470 | 8460 | 8580 | $^4A_2$ | 9603 | 9315 | 9703 | 10 142 | 10 855 | 10 047 | 10 737 |
| | | | | $^4E$ | 9521 | 9233 | 9974 | 10 195 | 11 662 | 12 557 | 11 379 |
| | | | | | 10 575 | 10 395 | 10 483 | 11 276 | 15 348 | 15 849 | 15 190 |
| $^4T_1(P)$ | 17 280 | 17 720 | 17 700 | $^4A_2$ | 22 727 | 22 458 | 22 511 | 22 495 | 22 809 | 21 749 | 22 638 |
| | 18 600 | 19 190 | 19 410 | $^4E$ | 22 494 | 22 469 | 21 895 | 21 487 | 24 214 | 24 465 | 23 961 |
| | | | | | 22 901 | 22 660 | 23 397 | 24 582 | 28 335 | 27 937 | 28 301 |

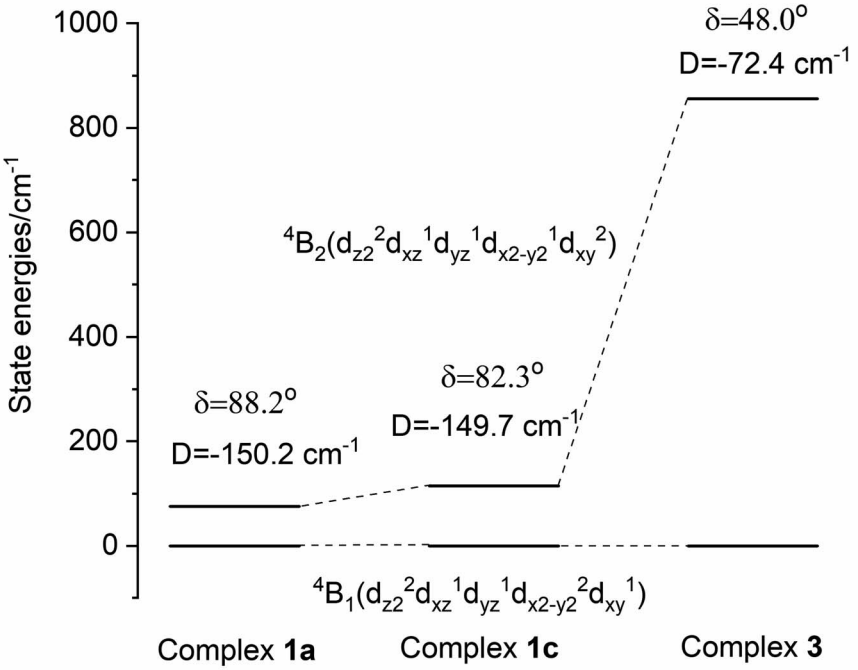


Fig. 8 Non-relativistic energies, ZFS parameter and dihedral angles for selected structures. The $^4B_2$ state has an energy smaller than the magnitude of spin–orbit coupling and therefore mixes strongly with the $^4B_1$ state.

spectroscopy is made in the section below (Table 2). Analysis of the scalar relativistic wave functions (Fig. 8) shows that the ground state is $^4B_1$ ($D_{2d}$ point group) dominated by the configuration $d_{z^2}^2 d_{x^2-y^2}^2 d_{xy}^1 d_{yz}^1 d_{xz}^1$ while the excited state is $^4B_2$ where one electron is excited from $d_{x^2-y^2}$ to $d_{xy}$ resulting in a configuration given by $d_{z^2}^2 d_{x^2-y^2}^1 d_{xy}^2 d_{yz}^1 d_{xz}^1$.

### Computed absorption spectra

The UV-Vis-NIR spectrum of solid **1** (Fig. 9) shows distinct features compared to the spectra of complexes **2** and **3** (Fig. 10). Complex **1** displays a sharp band at 17 280 $cm^{-1}$ with a shoulder peak around 18 600 $cm^{-1}$. The broad band extending from 12 500 $cm^{-1}$ to the NIR region (peak at 8470 $cm^{-1}$) probably comprises several transitions. Complexes **2** and **3** exhibit similar bands in their absorption spectra with distinct bands at 19 190 $cm^{-1}$, 17 720 $cm^{-1}$, 8460 $cm^{-1}$ (**2**) and at 19 410 $cm^{-1}$, 17 700 $cm^{-1}$, 8580 $cm^{-1}$ (**3**), respectively.

The CASSCF/NEVPT2 results predict excitations from the ground state with a character of $^4A_2(F)$ to the $^4T_2(F)$, $^4T_1(F)$ and $^4T_1(P)$ states ($T_d$ symmetry notations). The $^4A_2 \rightarrow {}^4T_2(F)$ transition is quite low in energy and is usually not seen in the spectrum of Co(II) complexes. Based on the CASSCF/NEVPT2 calculations it is possible to assign the bands observed in the ~8000 $cm^{-1}$ range as the excitation to the $^4T_1(F)$ states and the bands at ~17 000 $cm^{-1}$ as excitations to the $^4T_1(P)$ states. The overlap due to the broad nature of these peaks prevents any further resolution of the spectral assignment. The error range between theory and experiment for the $^4T_1(F)$ states is about 2500 $cm^{-1}$ and the error for the $^4T_1(P)$ states is about 5000 $cm^{-1}$; the closer proximity of the $^4T_1(P)$ to the charge transfer state is suspected to cause the larger error in the latter case.

The differences in the absorption spectra of complex **1** compared to complexes **2** and **3** are also seen in their computed spectra. On plotting the energies in a linear scale of energy, one can see that the d–d excitations lie in the 5000–20 000 $cm^{-1}$ energy range (Fig. 9 and 10). Above this range, the absorption is dominated by charge transfer transitions which are beyond the scope of the CASSCF wave function in minimal active space.

On average the theoretical absorption spectra are blue-shifted by about 2000 $cm^{-1}$ relative to the experimental spectra. This error is due to an underestimation of the dynamical correlation in the CASSCF wavefunction, which is not completely captured by the NEVPT2 correction. However, the intensities and splitting for excitations to both terms ($^4T_1(F)$ and $^4T_1(P)$) are predicted qualitatively correct. The unusual shape of the $^4P$ band in the experimental spectrum of **1** (whose solid sample contains all four structures **1a–1d**) results from a splitting of that band in structure **1d**. This is understood in terms of the large deviation of the dihedral angle $\delta$ of **1d** from the ideal 90° in $D_{2d}$ geometry.

### Ligand field analysis

*Ab initio* ligand field analysis *via* the *ab initio* ligand field theory (AILFT)[29] was employed to analyze the splitting of the d-orbitals. CASSCF energies and eigenvalues were used to reconstruct the ligand-field Hamiltonian. At the NEVPT2 level of theory, corrections to the energies of *d–d* transition have been taken into account. The ligand field matrix elements can be parametrized linearly in terms of ligand field parameters, the Racah parameters B and C and the 5 × 5 ligand field matrix, and hence these parameters can be obtained from a least-squares fit to their corresponding *ab initio* matrix counterparts. The Racah

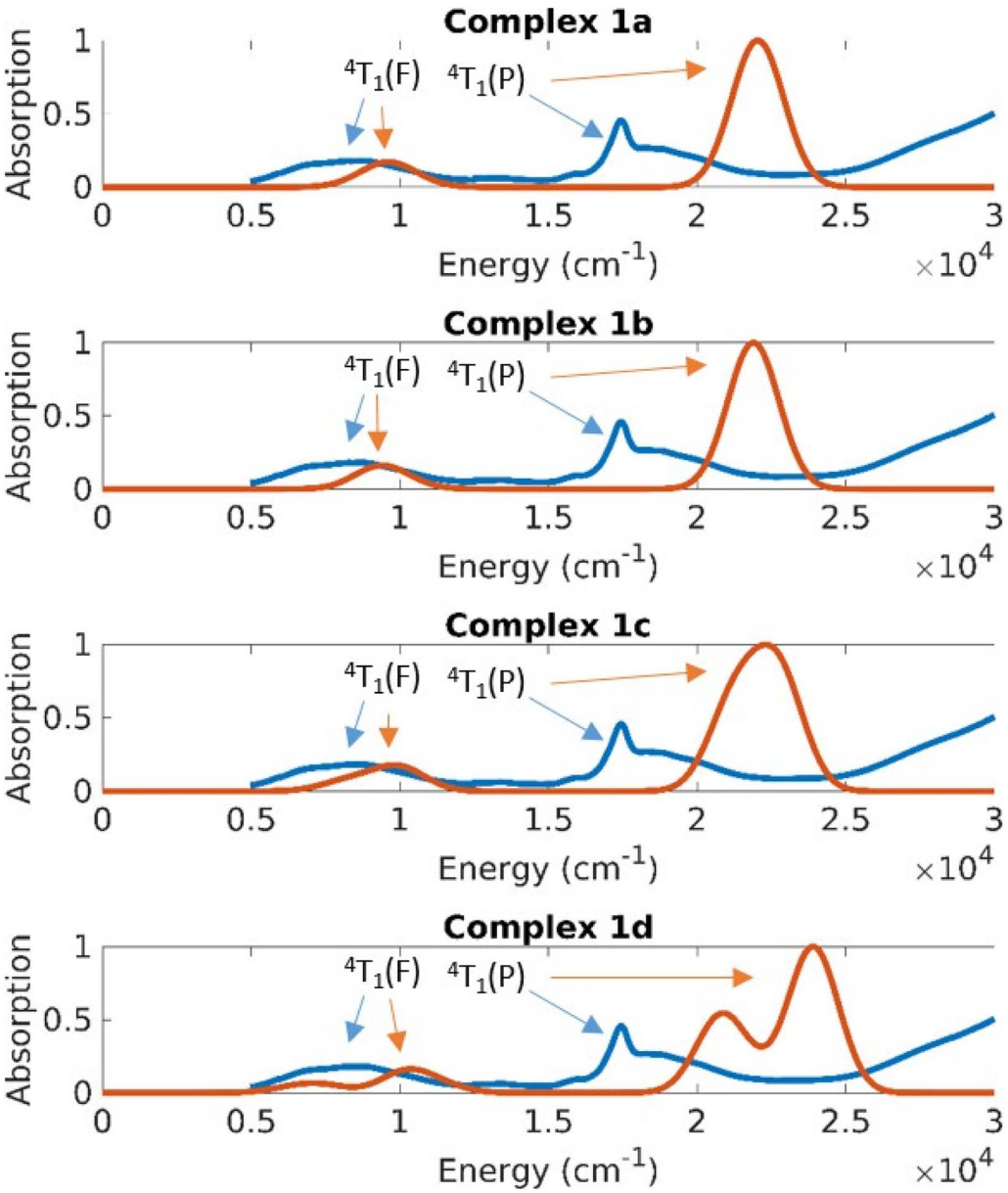


Fig. 9 Absorption spectra obtained by experiment (blue spectrum for solid **1**) and theory (red lines are calculated spectra for the different structures of **1**).

parameter A describes a mean repulsion common for all pairs of d-electrons. Therefore, the analyses of such systems focus on the parameters B and C, which account for the splitting of the free-ion states. Considering the fact that the spin–orbit coupling in these complexes is usually of the same form as the free ions, in the ligand-field analysis a single parameter ζ can be adjusted to fit spin–orbit coupling matrix elements.

*Ab initio* ligand field analyses have been performed for all the systems reported in this study, *viz.* for the structures of the four crystallographically independent molecules of **1** (**1a–1d**) as well as for **2** and **3**, in order to examine whether their different magnetic properties are associated with different Co–N bond character. As a next step in the analysis, the Racah parameters are extracted from fitting the AILFT matrix to the CASSCF/NEVPT2 eigenvectors and eigenvalues (as mentioned in the computational methods section; see ESI†). For parameters B and C the range obtained is 948.6 to 1006.8 cm$^{-1}$ and 3640.7 to 3770.3 cm$^{-1}$, respectively. Inspection of these parameters reveals no significant differences between the complexes. Furthermore, values for the effective nuclear charge parameter ζ are in the narrow range from 505.5 to 507.7 cm$^{-1}$. This confirms that qualitatively there is no difference in the electronic structures due to these parameters.

Further insight into the interaction between the metal ion and the ligands can be obtained by using a ligand field parametrization scheme, which is additive. For this purpose, the angular overlap model for analysis with the AOMX program has been used.[30] The nitrogen donor atoms are sp$^2$ hybridized, which means that one p orbital is available for out-of-plane π-bonding and one sp$^2$ orbital is available for σ-bonding. Thus the

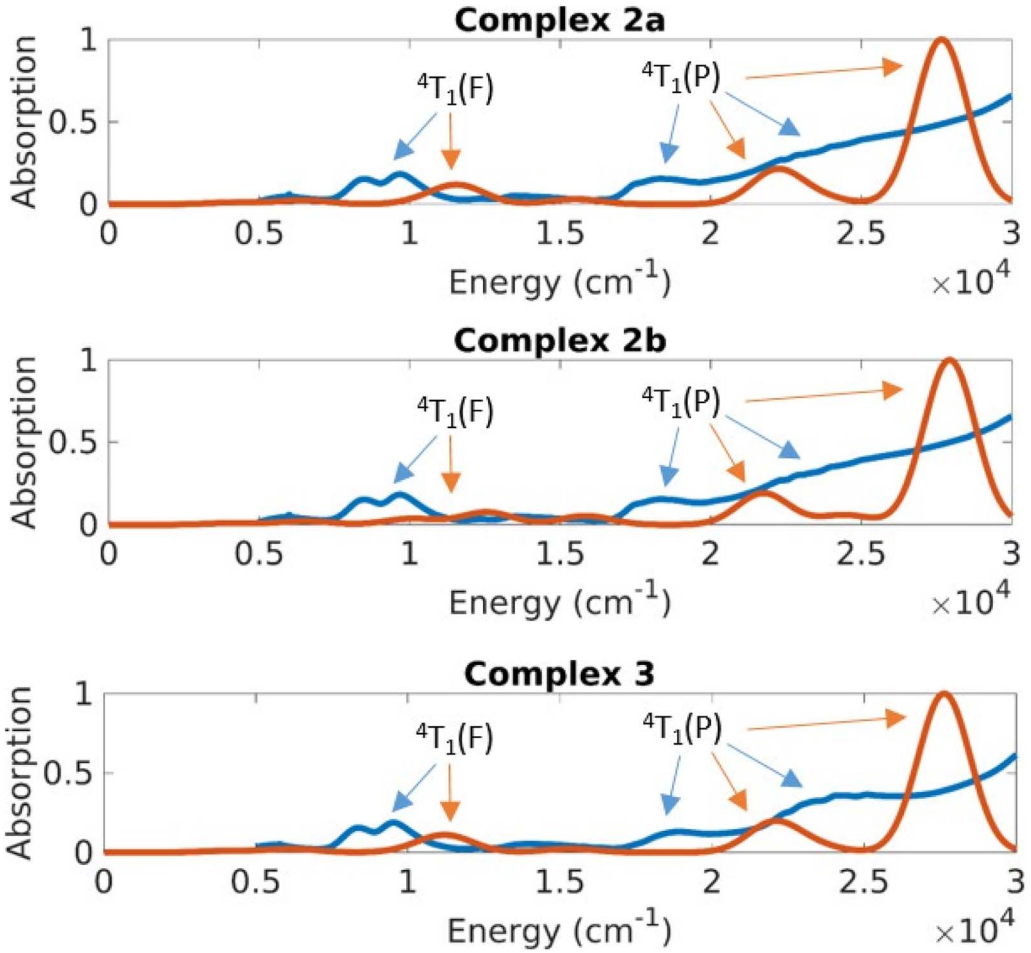


Fig. 10 Absorption spectra obtained by theory and experiment for solid-state measurement for the structures of complexes **2** and **3**. Red is the theoretical prediction for the different structures and blue is the experimental measurement.

expression describing the ligand field Hamiltonian is given by eqn (2)[31]

$$V_{ij} = \sum_{L=1}^{6} \sum_{\lambda=\sigma,\pi} F^L_{\lambda,i}(\theta_L, \phi_L) F^L_{\lambda,j}(\theta_L, \phi_L) e_\lambda \quad (2)$$

where $L$ denotes a ligand that has a position specified by the polar angles $\theta_L$ and $\phi_L$, and the AOM parameters are $e_\sigma$, $e_{\pi s}$ (out-of-plane π-bonding) and $e_{\pi c}$(in-plane π-bonding). With in-plane N ligand p-orbitals involved in strong bonds to carbon, the in-plane metal–ligand bonding for these systems is set to zero resulting in a model of two parameters. The angular overlap model parameters $e_\sigma$ and $e_{\pi s}$ were obtained by fitting the one electron ligand field matrices obtained by AILFT at the NEVPT2 level in ORCA; the $e_\sigma$ parameters are in the range of 5260 cm$^{-1}$ to 5987 cm$^{-1}$. In addition, the $e_{\pi s}$ parameters are in the range of 1546 cm$^{-1}$ to 1792 cm$^{-1}$. The analysis shows a minor standard deviation of up to 627 cm$^{-1}$ indicating that the variation in the AOM parameters is not statistically significant for both the $e_\sigma$ and $e_{\pi s}$ parameters. However, analytical expressions were derived for the angular overlap model and the

Table 3 Parameters extracted by the analysis of the CASSCF/NEVPT2 AILFT results. $D$ and $E/D$ parameters from effective Hamiltonian theory, the dihedral angle ($\delta$) and scalar relativistic energies of the lowest excited state ($\Delta E(^4B_1)$)

| | $B$ (cm$^{-1}$) | $C$ (cm$^{-1}$) | $e_\sigma$ (cm$^{-1}$)[32] | $e_{\pi s}$ (cm$^{-1}$)[32] | $\zeta$ (cm$^{-1}$) | $D$ (cm$^{-1}$) | $E/D$ | Dihedral angle $\delta$ (°) | Energy of the $^4B_2$ state (cm$^{-1}$) |
|---|---|---|---|---|---|---|---|---|---|
| **1a** | 949 | 3760 | 5389 | 1792 | 505 | −149.7 | 0.001 | 88.2 | 94 |
| **1b** | 950 | 3771 | 5273 | 1741 | 506 | −149.2 | 0.001 | 89.2 | 100 |
| **1c** | 951 | 3770 | 5260 | 1730 | 506 | −147.4 | 0.002 | 82.4 | 134 |
| **1d** | 964 | 3763 | 5321 | 1612 | 507 | −142.7 | 0.007 | 72.6 | 186 |
| **2a** | 1007 | 3666 | 5906 | 1756 | 507 | −73.8 | 0.082 | 48.8 | 928 |
| **2b** | 1006 | 3641 | 5987 | 1721 | 506 | −73.1 | 0.072 | 49.1 | 1013 |
| **3** | 998 | 3687 | 5756 | 1546 | 508 | −77.9 | 0.081 | 48.0 | 856 |

explicit dependence on the geometric and ligand field parameters is discussed in the next section. The above results are summarized in Table 3, which shows that the ligand $[^{F}L]^{2-}$ is indeed a strong σ and π donor and that the two N-donor atoms in the chelate are well modelled without having to consider phase coupling between them. Structure **1d** has values slightly different from those of the other three structures of complex **1** because its dihedral angle of 72.6° shows the strongest deviation from the ideal $D_{2d}$ angle of 90°.

### Computational correlation of structures and magnetic properties

The magnetization and magnetic susceptibility were calculated using the exact magnetic sublevels computed by the CASSCF/NEVPT2 calculations (S2). The theoretically predicted curves closely correspond to the experimental measurements (Fig. 2 and S38–S42†). The gradual tapering upwards of the graph at higher values is due to temperature-independent paramagnetism (TIP). Table 1 (*vide supra*) shows that the computed $g_z$ of complex **1** in all four computed structures (corresponding to the four crystallographically independent molecules **1a–1d** found in the unit cell of **1**) is in the range 3.53 to 3.48 while the $g_x$ and $g_y$ are in the range of 1.50 to 1.74. This anisotropy is much higher than those of complexes **2** and **3** where $g_z$ is in the range of 2.97 to 3.01 and the $g_x$ and $g_y$ values are in the range of 1.98 to 2.20.

Furthermore, starting from the $D_{2d}$ idealized geometry of complex **1** the dihedral angle $\delta$ was gradually swept in increments of 5°, and the resulting structures were then analyzed for the effect on $D$ and $E/D$. The black solid lines in Fig. 11a and b shows the variation of $D$ and $E/D$ in an idealized geometry upon variation of the dihedral angle $\delta$, while keeping the $\theta$ angle constant, in line with the rigidity of the *N*,*N*′-chelating ligand (the bite angle is $2\theta = 82°$); the black solid circles indicate the parameters $D$ and $E/D$ obtained from fitting the experimental SQUID data whereas those extracted from the CASSCF/NEVPT2 results of the different structures are indicated with open circles. It can be seen that the idealized geometry is in reasonable agreement with the calculations for the exact structures, which is, in turn, consistent with the parameters derived from the experimental measurements.

In the absence of an external magnetic field and in axial symmetry, the spin–orbit coupling and ligand field induce a splitting of the $S = 3/2$ state into two distinct pairs of Kramers doublets: $M_s = \pm 3/2$ and $M_s = \pm 1/2$ with an energy difference that is equal to twice the zero-field splitting parameter ($D$). When the $M_s = \pm 3/2$ state is lower in energy the $D$ value is said to be negative. In addition to the axial ligand field, an orthorhombic distortion can lead to the mixing of the $M_S = \pm 3/2$ and $M_S = \pm 1/2$ sublevels.

The magnetization and susceptibility curves also yield information regarding these $D$ and $E/D$ parameters using the spin Hamiltonian:

$$\hat{H}_{SH} = D\left[\hat{S}_z^{\,2} + \frac{E}{D}\left(\hat{S}_x^{\,2} - \hat{S}_y^{\,2}\right)\right] + g_{\parallel}\beta H_{\parallel}\hat{S}_z + g_{\perp}\beta H_{\perp}\left(\hat{S}_x + \hat{S}_y\right) \quad (3)$$

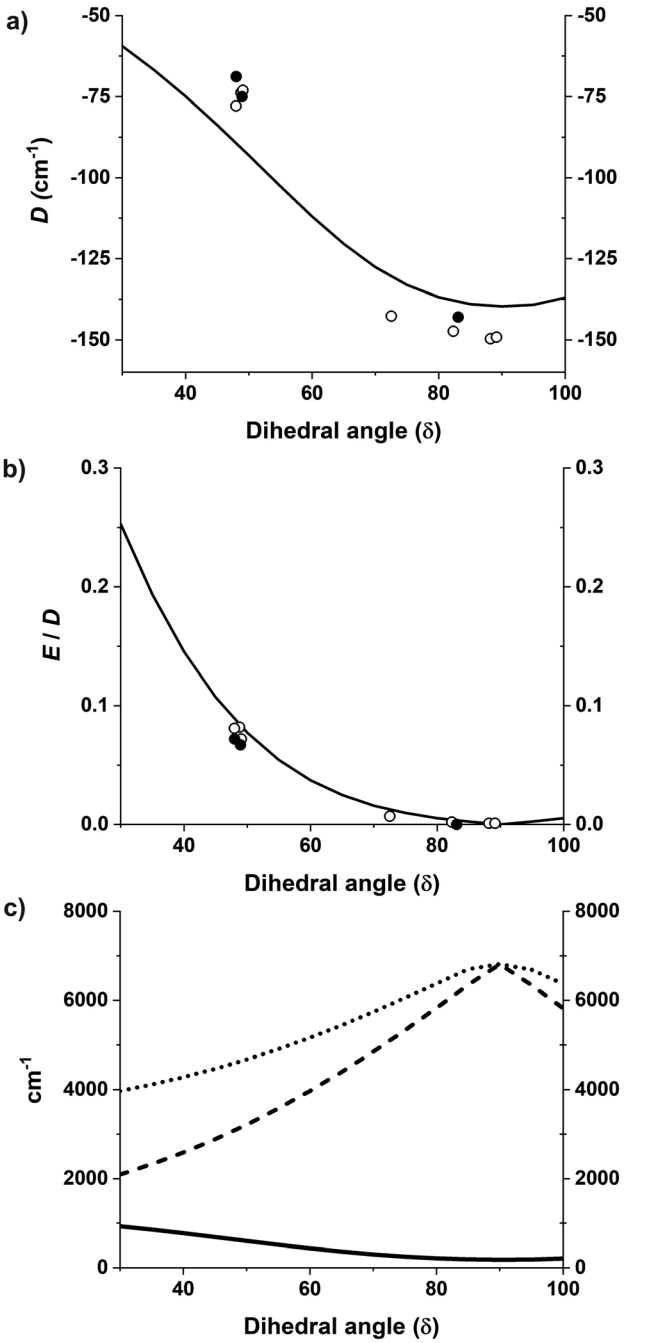


Fig. 11 (a and b) $D$ and $E/D$ plotted as a function of the dihedral angle where the solid black line shows the CASSCF calculations[33] with rotated geometries starting from an idealized $D_{2d}$ geometry. Open circles show the CASSCF/NEVPT2 results on the experimental structures and black solid circles show values obtained from fitting the experimental data. (c) Energies of the first, second, and third excited non-relativistic state energies as a function of the dihedral angle $\delta$ shown by solid black, dashed, and dotted lines respectively.

In these calculations, complex **1** gave $D$ and $E/D$ values in the range of −142.7 to −149.7 $cm^{-1}$ and 0.001 to 0.008, respectively, while complexes **2** and **3** gave $D$ and $E/D$ values in the range of −73.1 to −74.0 $cm^{-1}$ and 0.072 to 0.082, respectively, in line with the much better SMM properties of **1**; the calculated

parameters are compiled in Table 1. The values generated by the analysis of the CASSCF/NEVPT2 results are in line with the trends seen for these parameters derived from the experimental data.

The correlation between the dihedral angle $\delta$ and the first excitation is evident from the black curve in Fig. 11c. In all the studied complexes, the energy separation between the ground and the lowest excited state are of the same order of magnitude as the spin–orbit coupling constant (complexes **2a**, **2b** and **3**), inducing unquenched orbital momenta responsible for the negative $D$ for all complexes. With an energy separation much smaller in complexes **1a–1d** this results in the largest negative values of $D$ and is reflected in their SMM properties.

Using the angular overlap model, the one-electron ligand-field Hamiltonian was parametrized for a $D_2$ point group symmetry as per equations given in ESI Section S4.† Average values of the Racah parameters from AILFT fits at the NEVPT2 level and the spin–orbit coupling obtained from CASSCF were used to calculate the many-particle, relativistic ligand field Hamiltonian matrix within the basis of the $S = 3/2$ ground state. Using this space of magnetic sublevels we extracted the parameters of the zero-field splitting spin-Hamiltonian ($D$ and $E$) in dependence on the two structural parameters investigated here, *viz.* the dihedral angle ($\delta$) and bite angle ($2\theta$), as well as on the two angular overlap parameters $e_\sigma$ and $e_{\pi s}$. Two-dimensional slices showing correlations between the zero-field splitting $D$ and pairs of the parameters are presented in Fig. 12 and S86–S88;† they provide a basis for understanding the current system and predicting future systems of interest. The bite angle for the complexes in consideration in the current study is constant at about 82° due to the rigidity of the chelating ligand. Fig. 12 (left) shows the variation of $D$ as a function of $e_{\pi s}$ and $\delta$ using a fixed bite angle of 82° and the average value of $e_\sigma$ of all the complexes studied in this work, *i.e.* 5556 $cm^{-1}$. The zero-field splitting is rather sensitive to both parameters $e_{\pi s}$ and $\delta$, but the sensitivity varies across the range. Close to a dihedral angle of 90° the value of $D$ is more sensitive to the extent of the ligand π-bonding strength, whereas the sensitivity of $D$ with respect to the out-of-plane π-bonding is greatly reduced when the dihedral angle tends toward 50°. Likewise, at higher values of $e_{\pi s}$ the sensitivity to the dihedral angle is lower.

In order to analyze the effect of the dihedral angle $\delta$ and the bite angle $2\theta$ on $D$ values, both $e_\sigma$ and $e_{\pi s}$ were fixed to their average values for the present set of complexes, *viz.* to 5556 and 1700 $cm^{-1}$, respectively. Fig. 12 (right) shows that the $D$ value is highly sensitive to the ligand bite angle, and its value of 82° enforced by the $N,N'$ chelate ligand in the present series of complexes is close to optimal for maximizing the zero-field splitting. With a given bite angle $2\theta = 82°$, increasing the dihedral angle $\delta$ increases the magnitude of the zero-field splitting systematically up to about 90°. This result from the AOM scheme is in qualitative correspondence with the *ab initio* NEVPT2 calculations (Fig. 12).

The zero-field splitting was also analyzed with respect to variations in $e_\sigma$ and $e_{\pi s}$ for a fixed bite angle $2\theta$ of 82° and a dihedral angle $\delta$ of 90° (Fig. S86†). One can understand the effect of these parameters at a deeper level using the difference in the orbital energies of the $3d_{xy}$ and $3d_{x^2-y^2}$ orbitals (Fig. S88 and Section S80†) which are responsible for the energy separation between the $^4B_1$ ground state and the $^4B_2$ state. The one-electron Hamiltonian is diagonal for this geometry and thus the orbital energy gap reduces to the equation $E(3d_{xy}) - E(3d_{x^2-y^2}) = (0.55)e_\sigma - (1.72)e_{\pi s}$. Thus, with increasing $e_\sigma$ the orbital energy separation becomes greater, leading to a larger separation between the $^4B_1$ and $^4B_2$ states, which results in a lower magnitude of $D$ (as explained by perturbation theory, see Section 4.2 in ESI†). However, increasing $e_{\pi s}$ has a lowering effect on the orbital energy separation and therefore the magnitude of $D$ becomes larger with increasing $e_{\pi s}$. We also see from the equation that the effect of $e_{\pi s}$ is more pronounced than the effect of $e_\sigma$, and in the opposite direction.

Finally, the dependence of $D$ on $e_\sigma$ and the dihedral angle $\delta$ at a fixed $e_{\pi s} = 1700$ $cm^{-1}$ and a bite angle $2\theta$ of 82° shows (Fig. S87†) that the sensitivity with respect to the sigma bonding

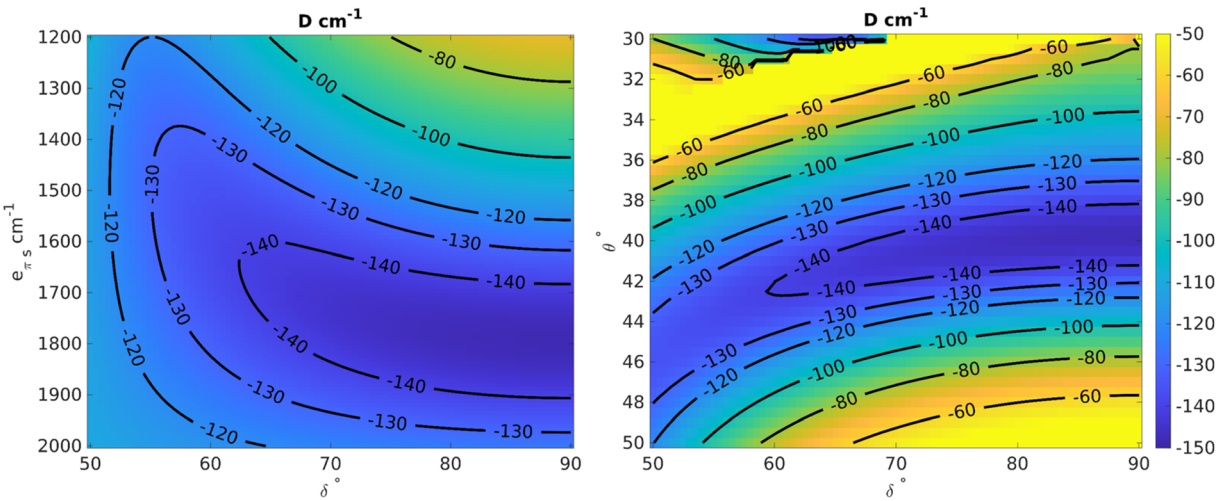


Fig. 12 Left: Variation of $D$ as a function of $e_\sigma$ and the dihedral angle $\delta$ at fixed values of bite angle $2\theta = 82°$ and average value of $e_\sigma = 5556$ $cm^{-1}$. Right: Variation of $D$ as a function of dihedral angle $\delta$ and bite angle at fixed average values of $e_{\pi s} = 1700$ $cm^{-1}$ and $e_\sigma = 5556$ $cm^{-1}$.

is highest at a dihedral angle of 90° whereas closer to 50° there is hardly any dependence of the zero-field splitting on $e_\sigma$. This further validates the choice of $\delta = 90°$ for the correlation shown in Fig. S86.†

To corroborate the viability of the proposed magneto-structural correlations, we examined a series of related Co(II) complexes previously reported, *viz.* Co(II) bis(sulfonamido) benzene complexes[11h,p] (**E** in Chart 2 and Table S9†) as well as Co(II) complexes with chelating oxamido backbone architecture and comparable bite angles (**D** and **F** in Charts 1 and 2, and Table S10†).[11i,j] In the former case, it was found that $D$ increases (from $-110$ cm$^{-1}$ to $-130$ cm$^{-1}$) with increasing dihedral angle $\delta$ (from 83.28° to 86.62°; Table S9†). A similar trend is observed in the case of Co(II) complexes with chelating oxamido backbone (Table S10†) where $D$ increases from $-107.3$ cm$^{-1}$ to $-128.2$ cm$^{-1}$ with the increase of dihedral angle from 87.49° to 89.32°. Deviations from the trend can likely be understood based on the effects of the different bite angles, cations, and electronic effects of the substituents at the ligand backbone.

## Conclusions

In summary, the use of a highly electron-withdrawing group ($-C_6F_5$) as a substituent on a chelating diamido ligand $[^FL]^{2-}$ led to the isolation of a family of rugged tetracoordinate Co(II) complexes $[^FL_2Co]^{2-}$. Depending on the cations used ($NBu_4^+$ in **1**, $PPh_4^+$ in **2**, $[K@18\text{-crown-6}]^+$ in **3**), pronounced variations of the dihedral twist angle $\delta$ between the N–Co–N′ chelate planes are observed for the crystalline compounds, with $\delta$ ranging from 48.0 to 89.2°. These structural variations translate into drastically different magnetic properties of solid materials. A close to the orthogonal disposition of the two *N*,*N*′-chelating ligands at the Co(II) ion, as found for **1**, proved advantageous for the SIM properties, increasing the magnetic anisotropy ($D = -143$ cm$^{-1}$) and raising the energy barrier for relaxation to above 400 K, with magnetic blocking of 4.0 K. In contrast, a smaller dihedral twist angle $\delta$ gives rise to much smaller anisotropy and a substantial rhombic component (large $E/D$), which adversely affects the slow relaxation dynamics. CASSCF/NEVPT2 calculations successfully reproduced the absorption spectra as well as the magnetic properties of the $[^FL_2Co]^{2-}$ complexes with different dihedral angles, including their magnetic susceptibility, VTVH signatures, and *g*-factors. Computationally sweeping the dihedral twist angle between the two N–Co–N′ chelate planes allowed to analyze the effect of structural variation on the $D$ and $E/D$ values of the system and to derive correlations between the energy of the first excited scalar-relativistic state and the zero-field splitting. Indeed, for tetracoordinate Co(II) complexes with two *N*,*N*′-chelating σ- and π-donor ligands an orthogonal situation, *viz.* a dihedral twist angle of 90°, leads to a small energy gap between the ground and first excited state, translating into the largest $D$ and a vanishing $E/D$. This differs from the conclusion reached for a series of bis-chelate $\{N_2O_2\}$ Co(II) SIMs with π-acceptor Schiff-base N-donors, for which it was proposed that both the axial and rhombic ZFS parameters $D$ and $E$ increase with increasing distortion towards a square-planar coordination geometry, *viz.* with smaller dihedral twist angle $\delta$.[20] In the present study a chelate bite angle $2\theta$ of around 80° is found to be most favorable, in line with the results of recent studies for related ligand types.[11f,g,11i] Furthermore, *ab initio* ligand field analyses with a fully analytical parametrization of the ligand field theory matrix now allowed to correlate the different magnetic properties not only with the structural but also with the bonding variations of the $[^FL_2Co]^{2-}$ molecules, *viz.* the two angular overlap parameters $e_\sigma$ and $e_{\pi s}$.

The findings of this work establish valuable design guidelines for the synthesis of Co(II) complexes with favorable SIM properties. In the present case, for magnetically diluted $[^FL_2Co](TBA)_2$ (**1**) with favorable (average) dihedral twist angle ($\delta \approx 83°$) and N–Co–N bite angle ($2\theta \approx 81°$), magnetic blocking has been observed up to 4.0 K with an open hysteresis up to 3.5 K at a sweep rate of 30 Oe s$^{-1}$, which is quite impressive for SIMs based on 3d metal ions. An additional benefit of these Co(II) complexes based on $[^FL]^{2-}$ is their increased air and moisture stability both in solid-state and solution, which we attribute to the decreased net charge density on the coordinating nitrogen atoms imparted by the electron-withdrawing $-C_6F_5$ substituents. The magnetic studies of complexes **1–3** in frozen solution evidence that the different structures of their anions $[^FL_2Co]^{2-}$ in the crystalline materials are governed by solid-state effects, and the presence of several molecules $[^FL_2Co]^{2-}$ in the unit cell of **1** with dihedral angles varying between 73° and 90° suggests that twisting of the bis(*N*,*N*′-chelated) core is relatively facile. This raises interesting perspectives for the targeted tuning or even switching of magnetic relaxation in bis(chelated) four-coordinate Co(II) complexes *via* manipulating their dihedral angle $\delta$ by additives and/or second sphere interactions.

## Experimental and computational methods

### Materials and instrumentation

The solvents employed in the synthesis were dried according to standard procedures and distilled prior to use. The syntheses of the complexes were carried out under a dry and inert nitrogen atmosphere. Unless otherwise stated, all chemicals used were purchased from commercial sources. $^1$H NMR and $^{13}$C NMR spectra were recorded on Bruker Avance 300 MHz and 400 MHz spectrometers at room temperature. Chemical shifts are reported in parts per million relative to residual proton and carbon signals of the solvent. Infrared spectra were recorded on a Cary 630 FTIR spectrometer equipped with Dial Path Technology and analysed by FTIR MicroLab software. UV-Vis-NIR spectra in solution and solid-state were recorded with a Varian Cary 5000 spectrophotometer. ESI-MS were collected using a Bruker HCT ultra spectrometer. Elemental analyses were performed by the analytical laboratory of the Institute of Inorganic Chemistry at the University of Göttingen using an Elementar Vario EL III instrument. Cyclic voltammetry (CV) experiments were performed with an Interface 1000B potentiostat at room temperature. A three-electrode setup was used with a glassy carbon working electrode, a platinum wire as a counter electrode, and a silver wire in 0.1 M $[TBA]PF_6$ solution

in acetonitrile as a pseudo-reference electrode. [TBA]$PF_6$ (0.1 M solution in MeCN) was used as the supporting electrolyte. Ferrocene was used as an internal standard, and the data were analyzed with Gamry Framework software.

### Synthesis protocols

**[$^F$L$_2$Co](TBA)$_2$ (1).** $^F$LH$_2$ (420 mg, 1.0 mmol) was taken in THF (20.0 mL) and solid KH (80 mg, 2.0 mmol) was added slowly to the solution leading to the immediate evolution of dihydrogen. The reaction mixture was allowed to stir overnight and solid anhydrous $CoCl_2$ (65 mg, 0.5 mmol) was added to the reaction mixture. The reaction mixture was stirred for 24 h to obtain an orange precipitate. Solid tetrabutylammonium bromide (354 mg, 1.1 mmol) was added to the reaction and it was allowed to stir for 24 h. The orange solution was allowed to settle, and the solution was filtered. The volume of the reaction mixture was reduced under vacuum and diethyl ether was allowed to diffuse. Pink-violet needle shapes shaped crystals were obtained within a few days. Yield: (470 mg, 68% based on Co). Elemental analysis calculated for $C_{60}H_{72}Co_1F_{20}N_6O_4$ C, 52.22; H, 5.26; N, 6.09. Found C 52.48; H 5.35; N 6.07. FTIR ($cm^{-1}$) 2965 (w), 2938 (w), 2877 (w), 1657 (w), 1616 (s), 1507 (s), 1496 (s), 1450 (m), 1371 (m), 1254 (s), 1127 (w), 1019 (m), 1001 (s), 979 (s), 893 (w), (m), 881 (w), 871 (w), 796 (w), 779 (w), 750 (w), 682 (w), 656 (w), 631 (w), 577 (w), 563 (w), 486 (w). ESI-MS (negative ion mode, in $CH_3CN$): $m/z$, 447.2 $[M–2TBA]^{2-}$, 1136.9 $[M–TBA]^-$. UV-Vis-NIR (in $CH_3CN$, $\lambda_{max}$ in nm) 571, 1038, 1185. UV-Vis-NIR (solid state, $\lambda_{max}$ in nm) 533, 547, 572, 626, 1127.

**[$^F$L$_2$Co](PPh$_4$)$_2$ (2).** $^F$LH$_2$ (420 mg, 1.0 mmol) was taken in THF (20.0 mL) and solid KH (80 mg, 2.0 mmol) was added slowly to the solution leading to the immediate evolution of dihydrogen. The reaction mixture was allowed to stir overnight followed by the addition of solid anhydrous $CoCl_2$ (65 mg, 0.5 mmol). The reaction mixture was stirred for 24 h to obtain an orange precipitate. Solid tetraphenylphosphonium chloride (412 mg, 1.1 mmol) was added to the reaction, and it was allowed to stir for 24 h. The orange solid was allowed to settle, and the solution was decanted. The solid was then dissolved in DMF and filtered. Diethyl ether was allowed to diffuse slowly into the DMF solution leading to the isolation of block-shaped orange crystals. Yield: (550 mg, 75% based on Co). Elemental analysis calculated for $C_{76}H_{40}Co_1F_{20}N_4O_4P_2$ C, 57.99; H, 2.56; N, 3.56. Found C 58.05; H 2.43; N 3.55. FTIR ($cm^{-1}$) 3058 (w), 3013 (w), 1658 (m), 1621 (s), 1587 (m), 1495 (s), 1485 (s), 1450 (m), 1442 (m), 1436 (s), 1362 (m), 1338 (w), 1310 (m), 1299 (w), 1245 (s),1188 (w), 1163 (w), 1135 (w), 1123 (w), 1107 (s), 1001 (s), 977 (s), 890 (w), 858 (w), 849 (w), 821 (w), 774 (w), 756 (m), 720 (s), 687 (s), 637 (w), 616 (w), 577 (w), 554 (w), 521 (s), 481 (w). ESI-MS (negative ion mode, in $CH_3CN$): $m/z$, 447.2 $[M–2PPh_4]^{2-}$, 1233.8 $[M–PPh_4]^-$. UV-Vis-NIR (in $CH_3CN$, $\lambda_{max}$ in nm) 571, 1038, 1185. UV-Vis-NIR (solid state, $\lambda_{max}$ in nm) 545, 740, 1032, 1175.

**[$^F$L$_2$Co(K@18C6)$_2$]·2Et$_2$O (3).** $^F$LH$_2$ (420 mg, 1.0 mmol) was taken in THF (20.0 mL) and solid KH (80 mg, 2.0 mmol) was added slowly to the solution leading to the immediate evolution of dihydrogen. The reaction mixture was allowed to stir overnight followed by the addition of solid anhydrous $CoCl_2$ (65 mg, 0.5 mmol). The reaction mixture was stirred for 24 h to obtain an orange precipitate. Solid 18-crown-6 (396 mg, 1.5 mmol) was added to the reaction, and it was allowed to stir for 24 h. The orange solid was then allowed to settle, and the solution was decanted. The solid was then washed with THF (10.0 mL) and dried. Block-shaped orange-yellow crystals of **1** were obtained by slow diffusion of diethyl ether into the DMF solution. Yield: (640 mg, 78% based on Co). Elemental analysis calculated for $C_{52}H_{48}Co_1F_{20}K_2N_4O_{16}$ C, 41.58; H, 3.22; N, 3.73. Found C 41.76; H 3.48; N 3.83. FTIR ($cm^{-1}$) 2888 (w), 2860 (w), 2829 (w), 1657 (m), 1625 (s), 1582 (s), 1498 (s), 1475 (m), 1453 (m), 1373 (m), 1351 (s), 1313 (s), 1285 (w), 1261 (s), 1251 (s), 1164 (w), 1105 (s), 1004 (s), 981 (s), 962 (s), 891 (w), 838 (m), 775 (w), 680 (w), 660 (w), 636 (w), 577 (w), 558 (w), 528 (w), 486 (w). ESI-MS (negative ion mode, in $CH_3CN$): $m/z$, 447.2 $[M–(K@18C6)_2–2Et_2O]^{2-}$, 933.6 $[M–K–(18C6)_2–2Et_2O]^-$. UV-Vis-NIR (in $CH_3CN$, $\lambda_{max}$ in nm) 571, 1038, 1185. UV-Vis-NIR (solid state, $\lambda_{max}$ in nm) 528, 713, 1050, 1192.

**[$^F$L$_2$Zn](TBA)$_2$ (4).** $^F$LH$_2$ (420 mg, 1.0 mmol) was taken in THF (20.0 mL) and solid KH (80 mg, 2.0 mmol) was added slowly to the solution leading to the immediate evolution of dihydrogen. The reaction mixture was allowed to stir overnight and solid anhydrous $ZnCl_2$ (68 mg, 0.5 mmol) was added to the reaction mixture. The colourless solution obtained was stirred at room temperature for 24 h. Solid tetrabutylammonium bromide (354 mg, 1.1 mmol) was added to the reaction and it was allowed to again stir for 24 h and filtered. The volume of the reaction mixture was reduced under vacuum and diethyl ether was allowed to diffuse. Colourless needle-shaped crystals were obtained within a few days. Yield: (510 mg, 74% based on Zn). Elemental analysis calculated for $C_{60}H_{72}F_{20}N_6O_4Zn_1$ C, 51.97; H, 5.23; N, 6.06. Found C 51.97; H 5.08; N 6.03. $^1$H NMR (400 MHz, $CD_3CN$) $\delta$ 3.08 (m, 16H), 1.57 (p, $J$ = 7.9 Hz, 16H), 1.32 (h, $J$ = 7.4 Hz, 16H), 0.94 (t, $J$ = 7.3 Hz, 24H), ppm. $^{13}$C NMR (101 MHz, $CD_3CN$) $\delta$ 165.67, 144.65 (m), 142.24 (m), 139.74 (m), 138.62 (m), 137.29 (m), 136.24 (m), 125.07 (m), 59.36, 24.33, 20.34, 13.75 ppm. $^{19}$F NMR (377 MHz, $CD_3CN$) $\delta$ −149.2 to −149.3 (m, 2F), −167.8 to −167.9 (m, 1F), −168.1–168.3 (m, 2F) ppm. FTIR ($cm^{-1}$) 2965 (w), 2938 (w), 2877 (w), 1658 (w), 1614 (s), 1509 (s), 1496 (s), 1452 (m), 1370 (m), 1311 (m), 1262 (s), 1131 (w), 1043 (w), 1020 (m), 1002 (s), 980 (s), 894 (w), 881 (w), 871 (w), 796 (w), 778 (w), 751 (w), 683 (w), 655 (w), 633 (w), 577 (w), 564 (m), 486 (w). ESI-MS (negative ion mode, in $CH_3CN$): 449.7 $[M–2TBA]^{2-}$, 1141.9 $[M–TBA]^-$.

**[$^F$L$_2$Zn](PPh$_4$)$_2$ (5).** $^F$LH$_2$ (420 mg, 1.0 mmol) was taken in THF (20.0 mL) and solid KH (80 mg, 2.0 mmol) was added slowly to the solution leading to the immediate evolution of dihydrogen. The reaction mixture was allowed to stir overnight followed by the addition of solid anhydrous $ZnCl_2$ (65 mg, 0.5 mmol). The reaction mixture was stirred for 24 h to obtain a white precipitate. Solid tetraphenylphosphonium chloride (412 mg, 1.1 mmol) was added to the reaction, and it was allowed to stir for 24 h. The solid was allowed to settle and the solution was decanted. The solid was then dissolved in DMF and filtered. Diethyl ether was allowed to diffuse slowly into the DMF solution leading to the isolation of block-shaped colourless crystals. Yield: (640 mg, 81% based on Zn). Elemental

analysis calculated for $C_{76}H_{40}F_{20}N_4O_4P_2Zn_1$ C, 57.76; H, 2.55; N, 3.55. Found C 57.78; H 2.55; N 3.58. FTIR ($cm^{-1}$) 3058 (w), 3012 (w), 1656 (m), 1621 (s), 1587 (w), 1495 (s), 1485 (s), 1452 (m), 1442 (m), 1436 (s), 1356 (m), 1338 (w), 1310 (m), 1299 (w), 1254 (s),1189 (w), 1164 (w), 1143 (w), 1135 (w), 1124 (w), 1108 (s), 1001 (s), 978 (s), 889 (m), 857 (w), 849 (w), 774 (w), 755 (m), 720 (s), 687 (s), 638 (w), 616 (w), 554 (w), 521 (s), 486 (w). $^1$H NMR (400 MHz, $CD_3CN$) $\delta$ 7.94–7.86 (m, 1H), 7.74–7.66 (m, 4H) ppm. $^{13}$C NMR (101 MHz, $CD_3CN$) $\delta$ 165.68, 144.57 (m), 142.19 (m), 139.65 (m), 138.69 (m), 137.27 (m), 136.38, 136.35, 136.04 (m), 135.75, 135.65, 131.37, 131.24, 125.04 (m), 119.39, 118.50 ppm. $^{19}$F NMR (282 MHz, $CD_3CN$) $\delta$ −149.1 to −149.4 (m, 2F), −167.7 to −167.9 (m, 1F), −168.0–168.2 (m, 2F) ppm. $^{31}$P NMR (162 MHz, $CD_3CN$) $\delta$ 22.9 ppm ESI-MS (negative ion mode, in $CH_3CN$): $m/z$, 449.7 $[M–2PPh_4]^{2-}$, 1238.8 $[M–PPh_4]^-$.

**$[^FL_2Zn(K@18C6)_2]\cdot 2Et_2O$ (6).** $^FLH_2$ (420 mg, 1.0 mmol) was taken in THF (20.0 mL) and solid KH (80 mg, 2.0 mmol) was added slowly to the solution leading to the immediate evolution of dihydrogen. The reaction mixture was allowed to stir overnight followed by the addition of solid anhydrous $ZnCl_2$ (68 mg, 0.5 mmol). The reaction mixture was stirred for 24 h to obtain a white precipitate. Solid 18-crown-6 (396 mg, 1.5 mmol) was added to the reaction, and it was allowed to stir for 24 h. The solid was allowed to settle and the solution was decanted. The solid was then washed with THF (10.0 mL) and dried. Block-shaped colourless crystals were obtained by slow diffusion of diethyl ether into the DMF solution. Yield: (620 mg, 80% based on Zn). Elemental analysis calculated for $C_{52}H_{48}F_{20}K_2N_4O_{16}Zn_1$ C, 41.40; H, 3.21; N, 3.71. Found C 41.65; H 3.22; N 3.73. FTIR ($cm^{-1}$) 2889 (w), 2861 (w), 2830 (w), 1656 (m), 1622 (s), 1507 (s), 1496 (s), 1474 (m), 1454 (m), 1373 (m), 1351 (s), 1316 (m), 1266 (s), 1252 (m), 1106 (s), 1006 (s), 980 (s), 961 (s), 892 (w), 838 (m), 773 (w), 685 (w), 658 (w), 636 (w), 577 (w), 558 (w), 527 (w), 486 (w). $^1$H NMR (400 MHz, $CD_3CN$) $\delta$ 3.55 (s, –$CH_2$) ppm. $^{13}$C NMR (101 MHz, DMF-$d_6$) $\delta$ 164.90, 143.98 (m), 141.56 (m), 138.88 (m), 137.67 (m), 136.42 (m), 135.20 (m), 124.86 (m), 70.21 ppm. $^{19}$F NMR (377 MHz, $CD_3CN$) $\delta$ −149.2 to −149.3 (m, 2F), −167.5 to −167.7 (m, 1F), −168.0–168.3 (m, 2F) ppm. FTIR ($cm^{-1}$) 2888 (w), 2860 (w), 2829 (w), 1657 (m), 1625 (s), 1498 (s), 1475 (m), 1453 (m), 1373 (m), 1351 (s), 1313 (m), 1285 (w), 1261 (s), 1251 (s), 1105 (s), 1004 (s), 981 (s), 962 (s), 891 (w), 838 (m), 775 (w), 680 (w), 660 (w), 636 (w), 577 (w), 558 (w), 528 (w), 485 (w). ESI-MS (negative ion mode, in $CH_3CN$): $m/z$, 447.2 $[M–(K@18C6)_2–2Et_2O]^{2-}$, 938.6 $[M–K–(18C6)_2–2Et_2O]^-$.

**Preparation of the diluted samples (1′), (1″), (2′), (2″), (3′), and (3″).** Magnetic dilution was performed by appropriately weighing the corresponding complexes. The solids were dissolved in dimethylformamide and the solution was stirred for one hour. Diethyl ether was allowed to diffuse into the solution over time leading to the isolation of homogenous crystals in quantitative yield.

## Single crystal structure determinations

Crystal data and details of the data collections are given in Tables S1 & S2.† X-ray data were collected on a STOE IPDS II or a BRUKER D8-QUEST diffractometer (monochromated Mo-K$\alpha$ radiation, $\lambda$ = 0.71073 Å) by use of $\omega$ or $\omega$ and $\phi$ scans at low temperature. The structures were solved with SHELXT and refined on $F^2$ using all reflections with SHELXL.[34] Non-hydrogen atoms were refined anisotropically. Hydrogen atoms were placed in calculated positions and assigned to an isotropic displacement parameter of 1.5 or 1.2 $U_{eq}(C)$.

Crystals of **1** could only be obtained in rather poor quality, which is especially evident by the high $R_{int}$ value. Furthermore, two ethyl groups of $NEt_4^+$ cations were found to be disordered (occupancy factors: 0.59(2)/0.41(2) & 0.53(2)/0.47(2)). SADI restraints were applied for two (O═)C–C(═O) bonds. Likewise, in case of the isostructural **4** ($a$ = 23.3421(13), $b$ = 25.4937(10), $c$ = 22.5825(11) Å, $\beta$ = 106.256(4)°, $P2/c$) the arrangement of the atoms could be established, but the overall quality of the structure determinations prevents a detailed discussion of the bonding parameters. In case of **2** a pair of ligands is disordered about two positions in both crystallographically independent molecules (occupancy factors: 0.8554(14)/0.1446(14) & 0.539(2)/0.461(2)). Fig. S36† emphasizes the disorder. In the second crystallographically independent molecule the cobalt atom resides on a center of inversion, so that ligand pairs are symmetry related. SAME and SIMU restraints have been applied to model the disorder. Crystals of **3** were found to be twinned (twin law: 0.899 −0.002 −0.199, 0.002 −1.001 0.004, −0.969 −0.010 −0.895). The BASF was refined to: 0.303(1). Each ligand in **5** was found to be disordered about two positions (occupancy factors: 0.648(2)/0.352(2) & 0.650(2)/0.350(2)). SAME and RIGU restraints and EADP constraints were applied to model the disorder. The disorder is comparable to the disorder observed in **2**. As in **3** crystals of **6** were found to be twinned (twin law: 0.906 0 −0.188, 0 −1 0, −0.953 0 −0.906). The BASF was refined to: 0.115(1). Face-indexed absorption corrections were performed numerically with the program X-RED[35] or in case of **1** by the multi-scan method with SADABS.[36]

## Magnetic measurements

Magnetic measurements were carried out with a Quantum-Design MPMS3 SQUID magnetometer equipped with a 7.0 T magnet. Direct current (dc) magnetic susceptibility measurements were performed under an applied DC field with powdered polycrystalline samples in the range from 210 K to 2 K. The powdered samples were packed in a polycarbonate or gelatine capsule and covered with low-viscosity perfluoropolyether-based inert oil Fomblin Y45 in a non-magnetic sample holder. Each raw data for the measured magnetic moment was corrected for the diamagnetic contribution of the capsules including the inert oil if used according to $M_{dia}(capsule) = \chi_g mH$, with an experimentally obtained gram susceptibility of the capsules including the inert oil. The diamagnetic contribution of the compounds was corrected using Pascal's constants. Experimental data were modelled with the julX_2S program[23] using a fitting procedure to the spin Hamiltonians in eqn (3). Alternating current (ac) susceptibility measurements were carried out in an oscillating AC field of 3.0 Oe and frequencies ranging from 0.1 to 1000 Hz.

## Theoretical calculations

Computations were carried out with the ORCA package[26] using coordinates obtained from the X-ray crystallographic structure

determinations. In the presence of several disordered forms, all structures were analyzed. The spectrum of the Hamiltonian was computed using the state-averaged complete active space self-consistent field method (SA-CASSCF)[27] with n-electron valence perturbation theory to second-order (NEVPT-2).[28] Scalar relativistic effects were taken into account *via* the Douglas–Kroll–Hess (DKH) method of second order.[37] Ahlrichs polarized def2-TZVPP basis sets[38] optimized for DKH method[39] were used for all calculations. Resolution of identity along with corresponding auxiliary basis set[40] were used to speed up calculations. An active space of seven electrons on five active was 3d molecular orbitals CAS(7,5) was employed. The $S = 3/2$ ($S = 1/2$) states of the free ion ($^4$F, $^4$P and $^2$P, $^2$D,$^2$F, $^2$G and $^2$H, respectively) give rise to ten quartets (fourty doublets) of the complex. Absorption spectra of the complex are plotted with the orca_mapspc utility. The zero-field splitting tensor **D** of the spin Hamiltonian[41] $\hat{H}_{SH} = \hat{\vec{S}}\mathbf{D}\hat{\vec{S}}$ was extracted using effective Hamiltonian theory from a mapping onto the full spin–orbit coupling of many particle energy eigenvalues and wavefunctions (more details are provided in the ESI†).

## Data availability

CCDC 2240414 (**1**), 2240415 (**2**), 2240416 (**3**), 2240417 (**5**) and 2240418 (**6**) contain the supplementary crystallographic data for this paper. All other data for this paper, including data from experimental methods and computational studies, are available at the Göttingen Research Online server at **https://doi.org/10.25625/BV9SCD**.

## Author contributions

SKG carried out the synthesis, spectroscopic characterization, magnetic measurements, and analyses. SVR carried out the theoretical modeling and calculations. SD and EB helped with magnetic data collection and analysis. SD helped with the in-house single-crystal X-ray data collection and analysis. MA, FN, and FM conceived the study and supervised the experiments and analyses. The manuscript was written through the contributions of all authors and all the authors have approved the final version of the manuscript.

## Conflicts of interest

The authors declare no conflict of interest.

## Acknowledgements

S. K. G. is associated with the DFG-funded Research Training Group BENCh (RTG 2455) funded by the Deutsche Forschungsgemeinschaft (DFG, German Research Foundation, project 389479699) and thanks the Alexander von Humboldt Foundation and the International Centre, University of Göttingen, for postdoctoral fellowships. F.M. acknowledges the University of Göttingen for basic support. Purchase of the SQUID magnetometer and the X-ray diffractometer was enabled by the Deutsche Forschungsgemeinschaft (DFG, German Research Foundation, project numbers INST 186/1329-1 FUGG and INST 186/1327-1 FUGG, respectively) and the Niedersächsische Ministerium für Wissenschaft und Kultur (MWK). S. V. R. and F. N. acknowledge support from the MPI für Kohlenforschung and the Max Planck Society.

## References

1 R. Sessoli, D. Gatteschi, A. Caneschi and M. A. Novak, *Nature*, 1993, **365**, 141–143.
2 (*a*) E. Coronado, P. Delhaès, D. Gatteschi and J. S. Miller, *Molecular magnetism: from molecular assemblies to the devices*, Springer, 1996; (*b*) R. A. Layfield, *Organometallics*, 2014, **33**, 1084–1099; (*c*) A. Caneschi, D. Gatteschi, R. Sessoli, A. L. Barra, L. C. Brunel and M. Guillot, *J. Am. Chem. Soc.*, 1991, **113**, 5873–5874.
3 (*a*) S. V. Rao, J. M. Ashtree and A. Soncini, *Phys. B*, 2020, **592**, 412237; (*b*) D. Gatteschi, R. Sessoli and J. Villain, *Molecular nanomagnets*, Oxford University Press, New York, 2011; (*c*) C. Cervetti, A. Rettori, M. G. Pini, A. Cornia, A. Repollés, F. Luis, M. Dressel, S. Rauschenbach, K. Kern, M. Burghard and L. Bogani, *Nat. Mater.*, 2016, **15**, 164–168; (*d*) M. Shiddiq, D. Komijani, Y. Duan, A. Gaita-Ariño, E. Coronado and S. Hill, *Nature*, 2016, **531**, 348–351; (*e*) L. Bogani and W. Wernsdorfer, *Nat. Mater.*, 2008, **7**, 179–186; (*f*) M. Urdampilleta, S. Klyatskaya, J. P. Cleuziou, M. Ruben and W. Wernsdorfer, *Nat. Mater.*, 2011, **10**, 502–506; (*g*) D. Aravena and E. Ruiz, *Dalton Trans.*, 2020, **49**, 9916–9928.
4 L. Thomas, F. Lionti, R. Ballou, D. Gatteschi, R. Sessoli and B. Barbara, *Nature*, 1996, **383**, 145–147.
5 (*a*) A. M. Ako, I. J. Hewitt, V. Mereacre, R. Clérac, W. Wernsdorfer, C. E. Anson and A. K. Powell, *Angew. Chem., Int. Ed.*, 2006, **45**, 4926–4929; (*b*) A. J. Tasiopoulos, A. Vinslava, W. Wernsdorfer, K. A. Abboud and G. Christou, *Angew. Chem., Int. Ed.*, 2004, **43**, 2117–2121; (*c*) M. Murugesu, M. Habrych, W. Wernsdorfer, K. A. Abboud and G. Christou, *J. Am. Chem. Soc.*, 2004, **126**, 4766–4767.
6 (*a*) F. Neese and E. I. Solomon, *Inorg. Chem.*, 1998, **37**, 6568–6582; (*b*) J. Cirera, E. Ruiz, S. Alvarez, F. Neese and J. Kortus, *Chem.–Eur. J.*, 2009, **15**, 4078–4087; (*c*) F. Neese and D. A. Pantazis, *Faraday Discuss.*, 2011, **148**, 229–238; (*d*) O. Waldmann, *Inorg. Chem.*, 2007, **46**, 10035–10037.
7 (*a*) A. Sarkar, S. Dey and G. Rajaraman, *Chem.–Eur. J.*, 2020, **26**, 14036–14058; (*b*) S. Tripathi, A. Dey, M. Shanmugam, R. S. Narayanan and V. Chandrasekhar, in *Organometallic Magnets*, ed. V. Chandrasekhar and F. Pointillart, Springer International Publishing, 2019, pp. 35–75; (*c*) S. Gómez-Coca, D. Aravena, R. Morales and E. Ruiz, *Coord. Chem. Rev.*, 2015, **289–290**, 379–392; (*d*) M. Murrie, *Chem. Soc. Rev.*, 2010, **39**, 1986–1995.
8 J. M. Zadrozny and J. R. Long, *J. Am. Chem. Soc.*, 2011, **133**, 20732–20734.
9 (*a*) X.-N. Yao, J.-Z. Du, Y.-Q. Zhang, X.-B. Leng, M.-W. Yang, S.-D. Jiang, Z.-X. Wang, Z.-W. Ouyang, L. Deng, B.-W. Wang and S. Gao, *J. Am. Chem. Soc.*, 2017, **139**, 373–380; (*b*) P. C. Bunting, M. Atanasov, E. Damgaard-Møller,

M. Perfetti, I. Crassee, M. Orlita, J. Overgaard, J. v. Slageren, F. Neese and J. R. Long, *Science*, 2018, **362**, eaat7319.

10 (*a*) Y.-F. Deng, Z. Wang, Z.-W. Ouyang, B. Yin, Z. Zheng and Y.-Z. Zheng, *Chem.–Eur. J.*, 2016, **22**, 14821–14825; (*b*) Y.-F. Deng, T. Han, B. Yin and Y.-Z. Zheng, *Inorg. Chem. Front.*, 2017, **4**, 1141–1148.

11 (*a*) E. A. Suturina, D. Maganas, E. Bill, M. Atanasov and F. Neese, *Inorg. Chem.*, 2015, **54**, 9948–9961; (*b*) E. A. Suturina, J. Nehrkorn, J. M. Zadrozny, J. Liu, M. Atanasov, T. Weyhermüller, D. Maganas, S. Hill, A. Schnegg, E. Bill, J. R. Long and F. Neese, *Inorg. Chem.*, 2017, **56**, 3102–3118; (*c*) D. Maganas, S. Sottini, P. Kyritsis, E. J. J. Groenen and F. Neese, *Inorg. Chem.*, 2011, **50**, 8741–8754; (*d*) S. Vaidya, S. Tewary, S. K. Singh, S. K. Langley, K. S. Murray, Y. Lan, W. Wernsdorfer, G. Rajaraman and M. Shanmugam, *Inorg. Chem.*, 2016, **55**, 9564–9578; (*e*) S. Tripathi, S. Vaidya, K. U. Ansari, N. Ahmed, E. Rivière, L. Spillecke, C. Koo, R. Klingeler, T. Mallah, G. Rajaraman and M. Shanmugam, *Inorg. Chem.*, 2019, **58**, 9085–9100; (*f*) E. Carl, S. Demeshko, F. Meyer and D. Stalke, *Chem.–Eur. J.*, 2015, **21**, 10109–10115; (*g*) C. M. Legendre, E. Damgaard-Møller, J. Overgaard and D. Stalke, *Eur. J. Inorg. Chem.*, 2021, **2021**, 3108–3114; (*h*) Y. Rechkemmer, F. D. Breitgoff, M. van der Meer, M. Atanasov, M. Hakl, M. Orlita, P. Neugebauer, F. Neese, B. Sarkar and J. van Slageren, *Nat. Commun.*, 2016, **7**, 10467; (*i*) M. Wang, H. J. Xu, T. M. Sun, H. H. Cui, Y.-Q. Zhang, L. Chen and Y. F. Tang, *J. Solid State Chem.*, 2021, **299**, 122209; (*j*) H.-H. Cui, F. Lu, X.-T. Chen, Y.-Q. Zhang, W. Tong and Z.-L. Xue, *Inorg. Chem.*, 2019, **58**, 12555–12564; (*k*) M. R. Saber and K. R. Dunbar, *Chem. Commun.*, 2014, **50**, 12266–12269; (*l*) X.-N. Yao, M.-W. Yang, J. Xiong, J.-J. Liu, C. Gao, Y.-S. Meng, S.-D. Jiang, B.-W. Wang and S. Gao, *Inorg. Chem. Front.*, 2017, **4**, 701–705; (*m*) J. M. Zadrozny, J. Telser and J. R. Long, *Polyhedron*, 2013, **64**, 209–217; (*n*) J. Vallejo, E. Pardo, M. Viciano-Chumillas, I. Castro, P. Amorós, M. Déniz, C. Ruiz-Pérez, C. Yuste-Vivas, J. Krzystek, M. Julve, F. Lloret and J. Cano, *Chem. Sci.*, 2017, **8**, 3694–3702; (*o*) R. Boča, J. Miklovič and J. Titiš, *Inorg. Chem.*, 2014, **53**, 2367–2369; (*p*) H. Bamberger, U. Albold, J. Dubnická Midlíková, C.-Y. Su, N. Deibel, D. Hunger, P. P. Hallmen, P. Neugebauer, J. Beerhues, S. Demeshko, F. Meyer, B. Sarkar and J. van Slageren, *Inorg. Chem.*, 2021, **60**, 2953–2963; (*q*) S. K. Gupta, H. H. Nielsen, A. M. Thiel, E. A. Klahn, E. Feng, H. B. Cao, T. C. Hansen, E. Lelièvre-Berna, A. Gukasov, I. Kibalin, S. Dechert, S. Demeshko, J. Overgaard and F. Meyer, *JACS Au*, 2023, **3**, 429–440; (*r*) T. Wu, Y.-Q. Zhai, Y.-F. Deng, W.-P. Chen, T. Zhang and Y.-Z. Zheng, *Dalton Trans.*, 2019, **48**, 15419–15426; (*s*) M. S. Fataftah, J. M. Zadrozny, D. M. Rogers and D. E. Freedman, *Inorg. Chem.*, 2014, **53**, 10716–10721; (*t*) D. Tu, D. Shao, H. Yan and C. Lu, *Chem. Commun.*, 2016, **52**, 14326–14329; (*u*) P. Kumar, D. J. SantaLucia, K. Kaniewska-Laskowska, S. V. Lindeman, A. Ozarowski, J. Krzystek, M. Ozerov, J. Telser, J. F. Berry and A. T. Fiedler, *Inorg. Chem.*, 2020, **59**, 16178–16193; (*v*) M. S. Fataftah, S. C. Coste, B. Vlaisavljevich, J. M. Zadrozny and D. E. Freedman, *Chem. Sci.*, 2016, **7**, 6160–6166.

12 C. Rajnák, J. Titiš, O. Fuhr, M. Ruben and R. Boča, *Inorg. Chem.*, 2014, **53**, 8200–8202.

13 (*a*) V. V. Novikov, A. A. Pavlov, Y. V. Nelyubina, M.-E. Boulon, O. A. Varzatskii, Y. Z. Voloshin and R. E. P. Winpenny, *J. Am. Chem. Soc.*, 2015, **137**, 9792–9795; (*b*) B. Yao, Y.-F. Deng, T. Li, J. Xiong, B.-W. Wang, Z. Zheng and Y.-Z. Zhang, *Inorg. Chem.*, 2018, **57**, 14047–14051; (*c*) J. Vallejo, I. Castro, R. Ruiz-García, J. Cano, M. Julve, F. Lloret, G. De Munno, W. Wernsdorfer and E. Pardo, *J. Am. Chem. Soc.*, 2012, **134**, 15704–15707; (*d*) M. R. Saber, M. K. Singh and K. R. Dunbar, *Chem. Commun.*, 2020, **56**, 8492–8495; (*e*) A. A. Pavlov, D. Y. Aleshin, S. A. Savkina, A. S. Belov, N. N. Efimov, J. Nehrkorn, M. Ozerov, Y. Z. Voloshin, Y. V. Nelyubina and V. V. Novikov, *ChemPhysChem*, 2019, **20**, 1001–1005; (*f*) Y.-Y. Zhu, C. Cui, Y.-Q. Zhang, J.-H. Jia, X. Guo, C. Gao, K. Qian, S.-D. Jiang, B.-W. Wang, Z.-M. Wang and S. Gao, *Chem. Sci.*, 2013, **4**, 1802–1806; (*g*) Y.-Z. Zhang, S. Gómez-Coca, A. J. Brown, M. R. Saber, X. Zhang and K. R. Dunbar, *Chem. Sci.*, 2016, **7**, 6519–6527; (*h*) P. K. Sahu, A. Mondal and S. Konar, *Dalton Trans.*, 2021, **50**, 3825–3831; (*i*) A. Landart-Gereka, M. M. Quesada-Moreno, I. F. Díaz-Ortega, H. Nojiri, M. Ozerov, J. Krzystek, M. A. Palacios and E. Colacio, *Inorg. Chem. Front.*, 2022, **9**, 2810–2831.

14 (*a*) L. Chen, J. Wang, J.-M. Wei, W. Wernsdorfer, X.-T. Chen, Y.-Q. Zhang, Y. Song and Z.-L. Xue, *J. Am. Chem. Soc.*, 2014, **136**, 12213–12216; (*b*) L. Rigamonti, N. Bridonneau, G. Poneti, L. Tesi, L. Sorace, D. Pinkowicz, J. Jover, E. Ruiz, R. Sessoli and A. Cornia, *Chem.–Eur. J.*, 2018, **24**, 8857–8868.

15 I. G. Rau, S. Baumann, S. Rusponi, F. Donati, S. Stepanow, L. Gragnaniello, J. Dreiser, C. Piamonteze, F. Nolting, S. Gangopadhyay, O. R. Albertini, R. M. Macfarlane, C. P. Lutz, B. A. Jones, P. Gambardella, A. J. Heinrich and H. Brune, *Science*, 2014, **344**, 988–992.

16 (*a*) S. Tripathi, S. Vaidya, N. Ahmed, E. Andreasen Klahn, H. Cao, L. Spillecke, C. Koo, S. Spachmann, R. Klingeler, G. Rajaraman, J. Overgaard and M. Shanmugam, *Cell Rep. Phys. Sci.*, 2021, **2**, 100404; (*b*) M. Craven, M. H. Nygaard, J. M. Zadrozny, J. R. Long and J. Overgaard, *Inorg. Chem.*, 2018, **57**, 6913–6920; (*c*) M. Atanasov and F. Neese, *J. Phys.: Conf. Ser.*, 2018, **1148**, 012006; (*d*) A. Lunghi and S. Sanvito, *J. Chem. Phys.*, 2020, **153**, 174113.

17 (*a*) T. J. Woods, M. F. Ballesteros-Rivas, S. Gómez-Coca, E. Ruiz and K. R. Dunbar, *J. Am. Chem. Soc.*, 2016, **138**, 16407–16416; (*b*) A. Sarkar, S. Tewary, S. Sinkar and G. Rajaraman, *Chem.–Asian J.*, 2019, **14**, 4696–4704; (*c*) L. Devkota, D. J. SantaLucia, A. M. Wheaton, A. J. Pienkos, S. V. Lindeman, J. Krzystek, M. Ozerov, J. F. Berry, J. Telser and A. T. Fiedler, *Inorg. Chem.*, 2023, **62**, 5984–6002; (*d*) Y. Chen, Q. Yang, G. Peng, Y.-Q. Zhang and X.-M. Ren, *Dalton Trans.*, 2021, **50**, 13830–13840; (*e*) S. Vaidya, S. K. Singh, P. Shukla, K. Ansari, G. Rajaraman and M. Shanmugam, *Chem.–Eur. J.*, 2017, **23**, 9546–9559; (*f*) A. K. Mondal, M. Sundararajan and S. Konar, *Dalton Trans.*, 2018, **47**, 3745–3754; (*g*) S. Gomez-Coca,

E. Cremades, N. Aliaga-Alcalde and E. Ruiz, *J. Am. Chem. Soc.*, 2013, **135**, 7010–7018; (*h*) R. Bruno, J. Vallejo, N. Marino, G. De Munno, J. Krzystek, J. Cano, E. Pardo and D. Armentano, *Inorg. Chem.*, 2017, **56**, 1857–1864; (*i*) F. Yang, Q. Zhou, Y. Zhang, G. Zeng, G. Li, Z. Shi, B. Wang and S. Feng, *Chem. Commun.*, 2013, **49**, 5289–5291; (*j*) M. Idešicová, J. Titiš, J. Krzystek and R. Boča, *Inorg. Chem.*, 2013, **52**, 9409–9417.

18 S. Vaidya, P. Shukla, S. Tripathi, E. Rivière, T. Mallah, G. Rajaraman and M. Shanmugam, *Inorg. Chem.*, 2018, **57**, 3371–3386.

19 S. Vaidya, A. Upadhyay, S. K. Singh, T. Gupta, S. Tewary, S. K. Langley, J. P. S. Walsh, K. S. Murray, G. Rajaraman and M. Shanmugam, *Chem. Commun.*, 2015, **51**, 3739–3742.

20 (*a*) M. H. Pohle, M. Böhme, T. Lohmiller, S. Ziegenbalg, L. Blechschmidt, H. Görls, A. Schnegg and W. Plass, *Chem.–Eur. J.*, 2023, **29**, e202202966; (*b*) S. Ziegenbalg, D. Hornig, H. Görls and W. Plass, *Inorg. Chem.*, 2016, **55**, 4047–4058; (*c*) M. Böhme, S. Ziegenbalg, A. Aliabadi, A. Schnegg, H. Görls and W. Plass, *Dalton Trans.*, 2018, **47**, 10861–10873.

21 K. Yamaguchi, G. Matsumura, N. Haga and K. Shudo, *Acta Crystallogr., Sect. C: Cryst. Struct. Commun.*, 1992, **48**, 558–559.

22 L. Yang, D. R. Powell and R. P. Houser, *Dalton Trans.*, 2007, 955–964.

23 E. Bill, *julX_2S, Program for Simulation of Molecular Magnetic Data*, Max-Planck Institute for Chemical Energy Conversion, Mülheim/Ruhr, Germany, 2014.

24 D. Reta and N. F. Chilton, *Phys. Chem. Chem. Phys.*, 2019, **21**, 23567–23575.

25 K. Chakarawet, P. C. Bunting and J. R. Long, *J. Am. Chem. Soc.*, 2018, **140**, 2058–2061.

26 (*a*) F. Neese, *Wiley Interdiscip. Rev.: Comput. Mol. Sci.*, 2012, **2**, 73–78; (*b*) F. Neese, *Wiley Interdiscip. Rev.: Comput. Mol. Sci.*, 2018, **8**, e1327; (*c*) F. Neese, F. Wennmohs, U. Becker and C. Riplinger, *J. Chem. Phys.*, 2020, **152**, 224108.

27 (*a*) P. Siegbahn, A. Heiberg, B. Roos and B. Levy, *Phys. Scr.*, 1980, **21**, 323–327; (*b*) P. E. M. Siegbahn, J. Almlöf, A. Heiberg and B. O. Roos, *J. Chem. Phys.*, 1981, **74**, 2384–2396; (*c*) B. O. Roos, P. R. Taylor and P. E. M. Sigbahn, *Chem. Phys.*, 1980, **48**, 157–173.

28 (*a*) C. Angeli, R. Cimiraglia, S. Evangelisti, T. Leininger and J.-P. Malrieu, *J. Chem. Phys.*, 2001, **114**, 10252–10264; (*b*) C. Angeli and R. Cimiraglia, *Theor. Chem. Acc.*, 2002, **107**, 313–317; (*c*) C. Angeli, R. Cimiraglia and J.-P. Malrieu, *Chem. Phys. Lett.*, 2001, **350**, 297–305.

29 (*a*) M. Atanasov, J. M. Zadrozny, J. R. Long and F. Neese, *Chem. Sci.*, 2013, **4**, 139–156; (*b*) M. Atanasov, D. Ganyushin, K. Sivalingam and F. Neese, *Molecular electronic structures of transition metal complexes II*, 2011, pp. 149–220.

30 H. Adamsky, *AOMX: A FORTRAN Program for the Calculation of dn terms within the Angular Overlap Model with Interelectronic Repulsion and Spin-Orbit Coupling*, Institute of Theoretical Chemistry, Heinrich-Heine-Univ., 1995.

31 C. E. Schäffer, *A perturbation representation of weak covalent bonding*, Springer, Berlin, 1968.

32 AOM parameters extracted from a fitting of the respective CASSCF/NEVPT2 one-electron AILFT matrices using the geometry of each complex determined by X-ray diffraction.

33 CASSCF values do not differ much from NEVPT2 and is therefore used to generate the curves for the several rotated versions of the idealized geometry reduce computational cost.

34 (*a*) G. Sheldrick, *Acta Crystallogr., Sect. A: Found. Adv.*, 2015, **71**, 3–8; (*b*) G. Sheldrick, *Acta Crystallogr., Sect. C: Struct. Chem.*, 2015, **71**, 3–8.

35 *X-RED*, STOE & CIE GmbH, Darmstadt, Germany, 2002.

36 *SADABS*, BRUKER AXS GmbH, Karlsruhe, Germany, 2016.

37 (*a*) A. Wolf, M. Reiher and B. A. Hess, *J. Chem. Phys.*, 2002, **117**, 9215–9226; (*b*) B. A. Hess, *Phys. Rev. A: At., Mol., Opt. Phys.*, 1986, **33**, 3742–3748; (*c*) M. Reiher and A. Wolf, *J. Chem. Phys.*, 2004, **121**, 10945–10956; (*d*) A. Wolf and M. Reiher, *J. Chem. Phys.*, 2006, **124**, 064102.

38 (*a*) F. Weigend and R. Ahlrichs, *Phys. Chem. Chem. Phys.*, 2005, **7**, 3297–3305; (*b*) A. Schäfer, H. Horn and R. Ahlrichs, *J. Chem. Phys.*, 1992, **97**, 2571–2577; (*c*) A. Schäfer, C. Huber and R. Ahlrichs, *J. Chem. Phys.*, 1994, **100**, 5829–5835.

39 D. A. Pantazis, X.-Y. Chen, C. R. Landis and F. Neese, *J. Chem. Theory Comput.*, 2008, **4**, 908–919.

40 F. Neese, *J. Chem. Phys.*, 2003, **119**, 9428–9443.

41 (*a*) F. Neese, L. Lang and V. G. Chilkuri, *Topology, Entanglement, and Strong Correlations*, 2020; (*b*) R. Maurice, R. Bastardis, C. d. Graaf, N. Suaud, T. Mallah and N. Guihéry, *J. Chem. Theory Comput.*, 2009, **5**, 2977–2984; (*c*) V. Vallet, L. Maron, C. Teichteil and J.-P. Flament, *J. Chem. Phys.*, 2000, **113**, 1391–1402.